nature materials

Article

https://doi.org/10.1038/s41563-024-01897-x

Elucidating chirality transfer in liquid crystals of viruses

Received: 7 April 2023

Accepted: 11 April 2024

Published online: 23 May 2024

Check for updates

Eric Grelet [1] ✉ & Maxime M. C. Tortora [2,3] ✉

Chirality is ubiquitous in nature across all length scales, with major implications spanning fields from biology, chemistry and physics to materials science. How chirality propagates from nanoscale building blocks to meso- and macroscopic helical structures remains an open issue. Here, working with a canonical system of filamentous viruses, we demonstrate that their self-assembly into chiral liquid crystal phases quantitatively results from the interplay between two main mechanisms of chirality transfer: electrostatic interactions from the helical charge patterns on the virus surface, and fluctuation-based helical deformations leading to viral backbone helicity. Our experimental and theoretical approach provides a comprehensive framework for deciphering how chirality is hierarchically and quantitatively propagated across spatial scales. Our work highlights the ways in which supramolecular helicity may arise from subtle chiral contributions of opposite handedness that act either cooperatively or competitively, thus accounting for the multiplicity of chiral behaviours observed for nearly identical molecular systems.

Understanding and controlling the propagation of chirality across length scales, from chiral molecular primary units such as molecules possessing asymmetric carbons to ordered helical superstructures and chiral bulk assemblies, is of paramount importance in multiple contexts encompassing the fields of biology, chemistry and physics as well as nanotechnology and materials science[1–6]. Among large-scale chiral patterns, the liquid crystalline organization known as the 'cholesteric phase' can be arguably considered as the quintessential helical assembly (Extended Data Fig. 1). Beyond widespread technological applications ranging from the display industry to smart windows[7,8], cholesteric structures are also ubiquitously found in biological matter—both in vivo, as found in some plant tissues and in the cuticles of arthropods such as beetles and crabs[9], and also in vitro in solutions of cholesterol derivatives[10], nucleic acids[11–13], viruses[14–16], amyloid fibrils[17], chitin[18], cellulose nanocrystals[19–21] and so on.

Despite considerable efforts over past decades[13,15,16,21–27], the mechanisms responsible for the hierarchical propagation of chirality—that is, the causal relationship between the microscopic properties of molecular building blocks and their emergent macroscopic structure—remain largely unresolved. The underlying difficulty is that chiral interactions are intrinsically weak. This can be illustrated by the fact that the preferred mutual twist angle between two adjacent particles found in standard cholesteric arrangements is typically a fraction of a degree. This should be compared to the average angle by which the rods locally fluctuate in such liquid crystalline phases, which is typically of the order of tens of degrees, two orders of magnitude larger[28]. Consequently, any model of the system that aims to predict the hierarchical transfer of chirality from the molecular level to larger helical structures requires a highly accurate description of the chiral interactions in order to reliably account for the magnitude and sense of the resulting helical periodicity.

In this work we study the cholesteric liquid crystalline phase formed by aqueous suspensions of filamentous viruses both experimentally and theoretically. These viruses, known as bacteriophages for their ability to infect bacteria, are widely used as a model system in genetic engineering due to their ease of modification[29–32]; in soft condensed matter as monodisperse rod-like model particles[28,33,34]; and in nanotechnology as versatile and functionalizable colloidal templates[31,35,36]. Here we demonstrate that their self-organization into

[1]Centre de Recherche Paul Pascal (CRPP, UMR 5031), Univ. Bordeaux, CNRS, Pessac, France. [2]Laboratoire de Biologie et Modélisation de la Cellule (LBMC, UMR 5239, Inserm 1293), Univ. Claude Bernard Lyon 1, ENS de Lyon, CNRS, Lyon, France. [3]Present address: Department of Quantitative and Computational Biology, University of Southern California, Los Angeles, CA, USA. ✉e-mail: eric.grelet@crpp.cnrs.fr; tortora@usc.edu

https://doi.org/10.1038/s41563-024-01897-x

the cholesteric liquid crystalline state quantitatively results from the interplay between three different contributions of chirality transfer: (1) steric repulsion between the screw-shaped capsids arising from the helical arrangement of coat proteins on the virus surface; (2) electrostatic interactions between the helical charge pattern on the virus surface; and (3) long-wavelength chiral deformations stemming from the virus flexibility and leading to a coherent supramolecular helical morphology of the virus backbone (Fig. 1).

These sources of chirality transfer are independently probed by tuning the ionic environment and by the chemical functionalization of two specific virus strains that form chiral nematic phases with opposite handednesses. They are confirmed by numerical models including a detailed atomistic description of the interparticle force field, accounting quantitatively for the full set of our experimental results.

Results and discussion

Filamentous bacteriophages of the Ff family are micrometre-long semi-flexible particles that are primarily composed of a single-stranded DNA around which about 3,000 copies of the major coat protein p8 are assembled in an overlapping, interdigitated helical structure (Fig. 1). Two closely related strains are used, M13 and Y21M, which are structurally and biologically very similar[30] and which bear a net negative charge in physiological conditions (Fig. 2). The primary difference, a single amino acid mutation occurring in the central region of the 50-amino-acid-long coat protein p8 (that is, at position 21), slightly alters the symmetry of the phage capsid (Methods), as shown by Marvin et al. with high-resolution X-ray diffraction[30,32]. The resulting three-dimensional atomistic structure of the M13 and Y21M virus capsids are deposited in the Protein Data Bank (PDB) under entry numbers 1IFI and 2C0W, respectively.

Both capsids display a main right-handed groove (Fig. 1) stemming from the helicoidal wrapping of the major coat proteins p8, whose thread angles differ: $\varphi = 39.85°$ for M13 and 43.15° for Y21M. A secondary thread can be identified, which has a right-handed helical symmetry for the M13 capsid ($\psi = 5.15°$, 1IFI model) but is achiral for Y21M due to its exact two-fold screw symmetry ($\psi = 0°$, 2C0W model). These subtle structural differences between the two viruses result in a large change in their stiffness (Methods): the M13 strain is semi-flexible with a persistence length L_p over contour length L_c ratio of $L_p/L_c \approx 3$, whereas Y21M is nearly rigid with $L_p/L_c \approx 11$ (Fig. 2)[37]. When dispersed in buffer solutions of controlled pH and ionic strength I_S (Methods), both rod-shaped virions exhibit the same liquid crystal phase sequence[14,34] and self-organize into the cholesteric phase where the helical twist occurs perpendicular to the average particle orientation as shown in Extended Data Fig. 1. The cholesteric ordering is characterized by its helical periodicity, or pitch P, which is defined as positive (negative) for right- (left-) handedness. It is worth mentioning that, despite the similarity in the structure of the phages, their cholesteric phases have opposite handednesses: left-handed for M13 and right-handed for Y21M (Extended Data Fig. 1)[16,37]. By varying the ionic conditions, the cholesteric pitch $|P|$ of both viral mutants increases with increasing the ionic strength I_S (refs. 14,16; Extended Data Fig. 2) and as pH decreases towards the isoelectric point of the virus, pI_E (Figs. 2 and 3). This sensitivity of the cholesteric pitch to modulations of either the range or the intensity of electrostatic interactions shows their major contributions in the cholesteric assembly.

Different mechanisms have been suggested to predict the value and sense of the cholesteric pitch from the molecular features of the chiral constituents. They mostly rely on two main classes of chiral intermolecular potentials: steric interactions based on hardcore repulsion at different length scales, ranging from local helical threads decorating rod-like particles to full helical shapes such as hard helices[22,26,38,39], and electrostatic interactions resulting from the helical charge distributions carried by the particles[16,25,40], which have been further generalized to also include chiral dispersion forces[24,41]. However, most of these theoretical approaches have been developed at a coarse-grained level aiming to both capture the key physical mechanisms and keep the calculations tractable. As a consequence, their limited accuracy may be insufficient to fully account for the complexity of real experimental systems and generally does not provide a quantitative agreement between model predictions and experimental measurements[16,23].

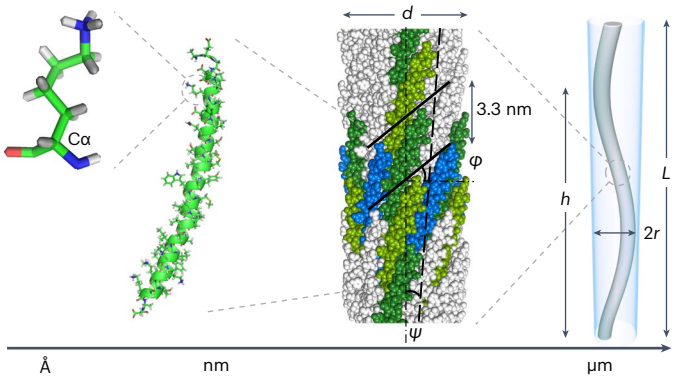

Fig. 1 | Structural chirality of filamentous viruses at various hierarchical scales, ranging from the asymmetry of Cα atoms of the amino acids of the major coat proteins p8, to the α-helical structure of these proteins and their helical arrangement on the virion surface. At the micrometre scale, the flexibility of the virus suggests the existence of suprahelical backbone deformation modes of radius r and internal helical pitch h, stemming from long-wavelength chiral fluctuations of the whole virus shape with end-to-end distance L. The atomistic models of both M13 and Y21M filamentous viruses are respectively derived from the 1IFI and 2C0W capsid structures[30,32] and deposited in the PDB. A primary right-handed thread angle resulting from the main groove formed by the major coat proteins p8 and indicated by black lines is found to be $\varphi < 45°$ for both mutants. A secondary groove and associated thread can be identified (black long-dashed lines) that has a right-handed helical symmetry for the M13 capsid ($\psi = 5.15°$, 1IFI model, as shown in the representation here) but is achiral for Y21M ($\psi = 0°$, 2C0W model). Different colours are used to highlight a few major coat proteins p8 and the associated symmetries of the capsid.

Straley was the first to propose a microscopic theory of the cholesteric phase based on an excluded-volume interaction by considering rod-like particles exhibiting additional chiral threads similar to screws[22]. The steric hindrance between two screw-like rods is minimal not when they are parallel to each other, but when they approach each other at a specific angle at which the chiral grooves can interpenetrate (Extended Data Fig. 3). Depending on the thread angle φ, the helical twist resulting from the optimal packing of right-handed screws may be either right-handed if $\varphi < 45°$ or left-handed if $\varphi > 45°$. This simple example illustrates the non-trivial relationship between the handedness of microscopic building blocks and that of their macroscopic helical assemblies, which can thus yield either homo-chiral ($\varphi < 45°$) or hetero-chiral ($\varphi > 45°$) structures depending on their detailed molecular morphology (Extended Data Fig. 3). Such steric-based chiral interactions have already been observed in experimental systems, for instance between helical nanofilaments of the B4 liquid crystalline phase[42]. As most biopolymers display helical charge patterns, models including electrostatic interactions have also been developed but have usually been limited to coarse-grained descriptions[16,40,41].

Here we go beyond coarse-grained approaches and introduce an electrostatic model built at the atomistic level and based on an all-atom representation of the ground-state conformation of the virus, in the absence of thermal fluctuations (Fig. 1). Our model provides an atomic-level description of the virion pair interaction energy U_{inter} that explicitly accounts for the screened electrostatic, steric and van der Waals forces involving each of the ~3×10^6 atoms within the virus capsid (Fig. 2). Potential parameters are set per amino acid and atom type using an iteration of the GROMOS force field optimized to reproduce

https://doi.org/10.1038/s41563-024-01897-x

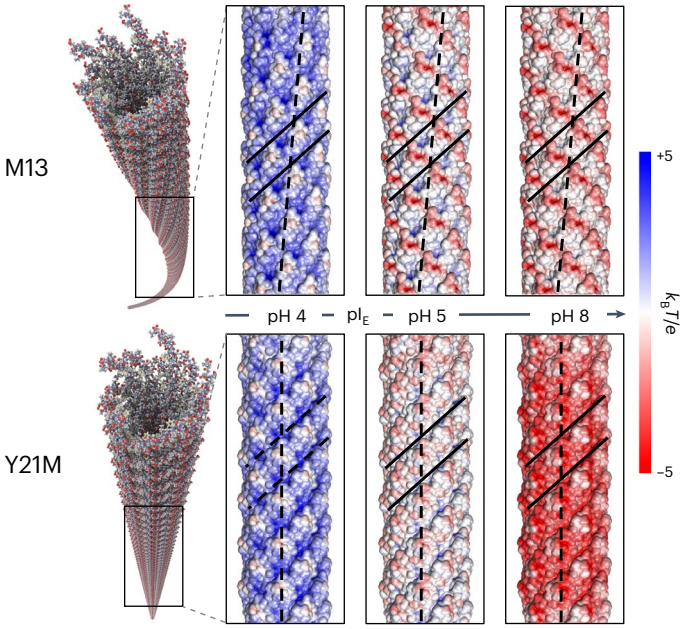

Fig. 2 | Atomistic representation of the semi-flexible M13 and stiff Y21M virions and pH dependence of their charge distribution calculated using Adaptive Poisson-Boltzmann Solver (APBS). The electrostatic surface potential of both viruses, rendered using the PyMOL software's APBS plugin[48], is shown to vary from negative (red) to positive (blue) by decreasing the pH below the virus isoelectric point pI$_E$. The two main threads identified on the virus capsid (as defined in Fig. 1) are indicated by continuous and long-dashed black lines, respectively. k_B, Boltzmann constant; T, temperature; e, electron charge.

the free enthalpy of solvation of biomolecular compounds, which includes a dependence on ionic content in the form of implicit-solvent electrostatic interactions (Methods)[43]. The atomistic representations of the Y21M and M13 capsids are respectively reconstructed from their 2C0W and 1IFI three-dimensional structures. The corresponding protonation states and charge distributions are inferred at various pH conditions using standard protein structure preparation software (Fig. 2 and Methods). As thermal fluctuations of the virion backbone are neglected, the electrostatic model is effectively developed in the high stiffness limit of the filamentous virus ($L_p \to \infty$). The cholesteric pitch P and twist elastic modulus K_{22} are then obtained from the minimization of the associated free energy $\mathcal{F}$ (Methods and Supplementary Sections I and II), and the results are shown in Fig. 3. An excellent quantitative agreement is found between theory and experiments for the Y21M virion, at both low and high pH values. The electrostatic model captures not only the sense and magnitude of the Y21M cholesteric helicity, but also its unwinding when the virus surface charge decreases. For the highest virus concentrations, the model slightly underestimates the resulting helicity of the system (Fig. 3). This likely arises from the second virial approximation underlying our model, which is expected to be increasingly inaccurate at higher virus volume fractions (Methods).

However, the electrostatic model does not account for the chiral phase behaviour of the M13 phage (Supplementary Section III), for which it strongly underestimates the chirality of the system. Thus, although the electrostatic model succeeds in capturing the experimentally observed cholesteric assembly of Y21M virions, another mechanism of chirality transfer has to be invoked in the case of M13 suspensions.

To further investigate the nature of the chiral interactions between viruses, a shell of neutral hydrophilic polymers (polyethylene glycol (PEG); Methods) is covalently grafted on both virion surfaces (Extended Data Fig. 4). The phase behaviour of the polymer-coated viruses (M13-PEG and Y21M-PEG) becomes independent of ionic strength at a high salt concentration[44]. In contrast to pristine viruses, whose colloidal stability relies on electrostatic repulsion and who therefore aggregate at the isoelectric point pI$_E$, PEGylated viruses are sterically stabilized and can then be studied at varying pH values (Extended Data Fig. 4). This includes the range close to the isoelectric point pI$_E$, where no net electric charge remains on the virus surface and therefore the electrostatic interactions vanish. Interestingly, in these conditions, a left-handed cholesteric phase still persists for the M13-PEG system at pI$_E$, whereas Y21M-PEG suspensions exhibit a nematic phase as expected in the absence of electrostatic interactions (Fig. 4). This implies that another general mechanism driving the chirality transfer for the M13 and M13-PEG phages needs to be considered. This independence from the electrostatic interactions leads to a cholesteric pitch that does not depend on ionic strength, as shown in Fig. 4b. Furthermore, the cholesteric pitch values found for M13 and M13-PEG are nearly identical when the colloidal stability is preserved (that is, at pH 8; Fig. 4a) and the virus concentration is rescaled by the binodal concentration associated with the stability limit of the isotropic phase, C_{iso}. This indicates that the mechanism of chirality transfer for M13 and M13-PEG to the cholesteric ordering is not sensitive to the structural details and symmetries of the phage surface, and occurs at a much higher length scale than the atomic level. A key difference between the two virus strains is their stiffness: M13 is semi-flexible whereas Y21M is a stiff colloidal rod (Methods). Together, these observations suggest a mechanism of chirality transfer based on long-wavelength helical fluctuations of the virus backbone, which we will henceforth refer to as the 'suprahelix model'[15,27].

In detail, the suprahelix model accounts for the ability of the virion flexibility to promote long-wavelength chiral deformation modes due to thermal fluctuations, leading to a coherent helical morphology

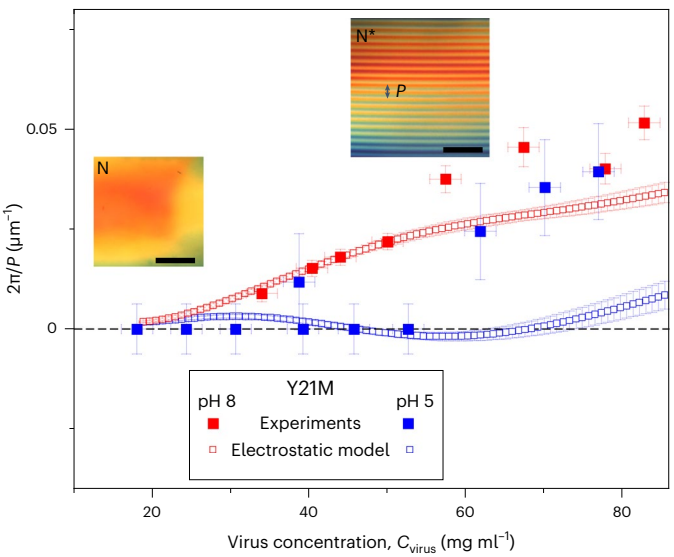

Fig. 3 | Cholesteric to nematic crossover by decreasing charge fully accounted for by the electrostatic model in Y21M virus suspensions. At low virus charge, that is, at pH 5 close to pI$_E$ (filled blue symbols), the cholesteric pitch unwinds by decreasing virus concentration until reaching the nematic phase ($2\pi/P = 0$), as illustrated by the two polarization micrographs showing the absence in the nematic (N, left inset) and the presence in the cholesteric (N*, right inset) of fingerprints (scale bars, 250 μm). By contrast, for highly charged viral rods at pH 8 (filled red symbols), a cholesteric phase of smaller pitch $|P|$ is observed across the whole liquid crystalline range. For both conditions of pH, the ionic strength is fixed at I_S = 110 mM. The electrostatic model (open symbols) quantitatively accounts for the experimental results of stiff Y21M in the dilute range of the cholesteric organization both at low and high charges (pH 5 and 8, respectively). Error bars are determined as detailed in Methods.

https://doi.org/10.1038/s41563-024-01897-x

spanning the entire virus shape[15]. While little to no primary proof of such a helical conformation has been reported[35], we provide here indirect experimental evidence for the formation of helical supramolecular self-assemblies from cholesteric suspensions of filamentous viruses under depletion interactions (Extended Data Fig. 5). These helical structures are reminiscent of the helical morphology assumed to arise from the backbone fluctuations of individual viruses in the suprahelix model and therefore strongly support this hypothesis. As the full mechanical modelling of filamentous phages over experimentally relevant timescales remains computationally inaccessible to standard atomistic simulations, we approximate these helical deformation modes by a mean effective backbone conformation, described by a hard helix of radius r and internal pitch h (Fig. 1). In this framework, $h \gg L_c$ indicates that the internal helical periodicity may far exceed the full length of an individual virus, giving rise to a weakly curved, 'suprahelical' higher-order shape[38].

Although the link between ground-state and fluctuation-induced chirality is generally non-trivial[27], the left-handed phases displayed by the more flexible M13 phages (Extended Data Fig. 1) suggest that the corresponding backbone deformations should be predominantly right-handed, in agreement with simple geometric arguments governing the self-assembly of weakly curled helices (Fig. 1 and Extended Data Fig. 3). Based on the 'tube' model of polymer deflection, Supplementary Section IV shows that the resulting suprahelical conformation may then be expressed in terms of the internal pitch h as the sole adjustable parameter for a given virion persistence length L_p. The cholesteric pitch P and the twist elastic constants K_{22} are also obtained for this model from the minimization of the free energy $\mathcal{F}$ associated with these weakly curled suprahelices interacting pairwise through hardcore repulsion. The results are shown in Figs. 4b and 5, where the internal pitch h of the suprahelical conformation has been set such that $h = 2.8L_p$. The PEGylation of viruses is limited to about 10% of the capsid proteins, so that the grafted polymers may change only the surface properties of the viruses and do not alter their internal structures (Methods), leading to the same persistence length—and therefore similar helical deformation amplitudes—for pristine and PEGylated virions. The difference between the persistence lengths of the M13 and Y21M phages is then sufficient to account, with $h = 2.8L_p$, for the magnitude and sign of the M13-PEG cholesteric pitch, as well as for the nematic-like behaviour (diverging pitch P) of the Y21M-PEG suspensions (Fig. 4). This mechanism of chirality transfer, based on long-wavelength helical deformations of the whole virus shape, relies mostly on excluded-volume interactions and may be shown, using scaling arguments, to depend solely on the ratio $\Phi/\Phi_{iso} \equiv C_{virus}/C_{iso}$ for a fixed particle length L_c with Φ the volume fraction of virus suspensions and where $_{iso}$ indicating the isotropic binodal point (Supplementary Section V).

In light of the vanishingly small values of $2\pi/P$ associated with the electrostatic model of ground-state M13 conformations (Supplementary Section III), let us postulate that the effects of the detailed chiral surface charge distribution on the cholesteric assembly of thermalized viruses may be neglected. We may then simply consider the viruses as uniformly charged (helical) rods, whose liquid crystalline behaviour can be remapped to that of a hard-body system with a charge- and ionic-strength-dependent effective diameter $d_{eff} > d$, where d is the bare rod diameter (ref. 45). Renormalizing the M13 virus concentrations by the corresponding binodal values C_{iso} at different ionic strengths (Extended Data Fig. 2), the inverse cholesteric pitch P of both charged M13 and PEGylated M13-PEG is indeed found to collapse onto a unique master curve (Fig. 5), quantitatively accounted for by the suprahelix model with $h = 2.8L_p$. Thus, contrary to the case of Y21M viruses where the local symmetry and details of the surface charge distribution matter, the existence of this master curve for M13 viruses proves the irrelevance of these local features for chirality propagation in the cholesteric phase, as quantitatively evidenced by the chiral potential of mean force (Supplementary Section VI). Furthermore, this master curve demonstrates that the origin of their chirality instead lies in long-wavelength helicoidal deformation modes, which are nearly not affected by PEGylation or changes in ionic conditions.

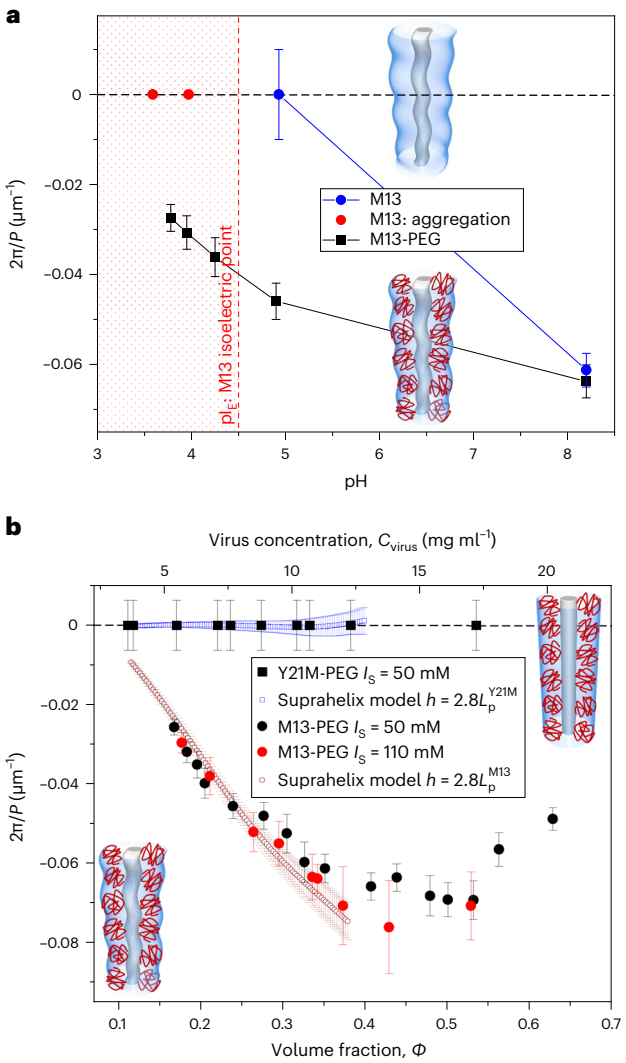

Fig. 4 | Cholesteric ordering in sterically stabilized semi-flexible viruses and suprahelix model. a, pH dependence of the inverse of the cholesteric pitch P in M13 (concentration $C_{M13} = 42$ mg ml^{-1}) and M13-PEG ($C_{M13\text{-}PEG} = 10.5$ mg ml^{-1}) suspensions at $I_S = 110$ mM. Each concentration is chosen in the fully liquid crystalline regime such that $C_{virus}/C_{iso} \approx 2$, where C_{iso} is the isotropic binodal concentration. As the pH is decreased below the isoelectric point pI_E (red dotted area), colloidal aggregation is observed in pristine M13 suspensions (red symbols). By contrast, sterically stabilized semi-flexible M13-PEG virions (filled black squares) still exhibit a left-handed cholesteric phase at, and below, the isoelectric point pI_E. **b**, Influence of viral rod flexibility on the inverse cholesteric pitch P in PEGylated virus suspensions. The semi-flexible M13-PEG system with a persistence length $L_p^{M13} \approx 3L_c$ (with L_c the virion contour length, and $L_c \approx L_c^{M13} \approx L_c^{Y21M}$) exhibits a cholesteric phase whose pitch (filled circles) is mostly independent of ionic strength I_S at a high enough salt concentration, whereas the stiff Y21M-PEG ($L_p^{Y21M} \approx 11L_c$) has a nematic-like behaviour (square symbols) without any observable chirality propagation. Our model of suprahelical backbone deformations with an internal pitch of $h = 2.8L_p$, as described in the main text, is able to account quantitatively for the chiral behaviour of stiff and semi-flexible PEGylated viruses. Error bars are determined as detailed in Methods. Insets are schematic representations of stiff (straight) and flexible virus mutants and of their effective electrostatic or steric (with grafted PEG polymers depicted in red) diameter.

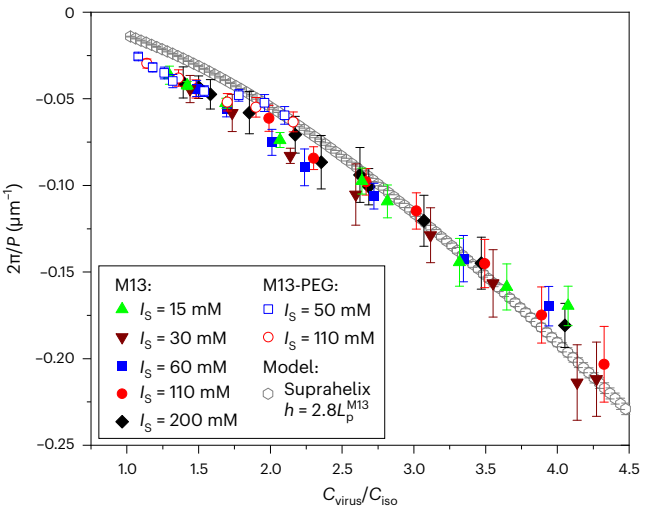

Fig. 5 | Master curve of the cholesteric pitch *P* for semi-flexible viruses accounted for by the suprahelix model. After renormalization of the particle concentration by the binodal value corresponding to the stability limit of the isotropic phase C_{iso}, the inverse cholesteric pitches P of both PEGylated M13-PEG limited to the dilute regime and charged M13 for all probed ionic strengths (raw data in Extended Data Fig. 2) collapse onto a unique master curve. All renormalized data are accounted for by the suprahelix model with an internal helical pitch of $h = 2.8L_p$. The binodal value C_{iso} used for the normalization of the theoretical model is corrected for rod flexibility[49]. The fact that C_{iso} is solely a function of the particle features (d, L_c and L_p)[28,49] indicates that the mechanism of chirality transfer of semi-flexible virions is mostly entropy driven, as explicitly demonstrated in Supplementary Section V. Error bars are determined as detailed in Methods.

Conclusion and outlook

We have extensively investigated the origin of chirality in liquid crystals of viruses—a question that has largely eluded scientists for more than two decades[15]. Through the fine tuning of experimental assembly conditions, combined with the development of quantitative atomistic models of the virus capsid, we are able to elucidate the mechanistic basis of chirality transfer for two distinct phages, M13 and Y21M, that, despite their high structural similarity, exhibit cholesteric phases of opposite handedness. The exquisite level of control over the molecular structure of the particles provided by these virus systems enables us to demonstrate that their surprising diversity of cholesteric behaviours stems from a subtle competition between thermal fluctuations, steric repulsion and electrostatic forces. For stiff Y21M virus strains, whose high bending rigidity largely suppresses conformational fluctuations away from a straight, rod-like backbone shape, we find that the cholesteric behaviour may be quantitatively attributed to local electrostatic interactions, which are highly sensitive to both ionic content and the detailed atomic symmetries of the capsids. This conclusion qualitatively mirrors the findings of previous studies of various biopolymers including chitin[46] and cellulose nanocrystals[20]. However, in contrast to these broadly studied colloidal cholesteric systems, we report that the phase chirality of Y21M solutions decreases by reducing the strength of electrostatic interactions through the modulation of the pH and ionic environment. We attribute this behaviour to the well-defined linear morphology of the virus backbone, whose molecular chirality originates primarily from the subtle helical distribution of surface charges around the symmetry axes of the capsid (Fig. 2), and whose effects may be increasingly screened by reducing the range and magnitude of the associated electrostatic forces (Supplementary Section VI). This ideal rod-like architecture differs from the size and shape polydispersity characterizing cholesteric assemblies of other bio-colloids such as chitin and cellulose, whose detailed atomistic structures remain challenging to resolve at the molecular level, as discussed further in the following.

Conversely, for the more flexible M13 variant, our results reveal that phase chirality instead proceeds from weak, fluctuation-induced suprahelical deformations of the virus backbone, and it is chiefly driven by steric, rather than electrostatic, interactions. This conclusion mirrors recent findings in cholesteric systems of DNA origamis[27] and is evidenced by the collapse of the cholesteric pitches measured in various experimental conditions onto a unique master function of the rescaled concentration C/C_{iso} (Fig. 5). In this context, the apparent unwinding of the cholesteric pitch with increasing ionic strengths at fixed (absolute) concentration C may be quantitatively ascribed to the variations of the virion effective diameter d_{eff} (in the limit where the Debye screening length $\kappa^{-1} \ll L_c$), and is largely independent of the specific capsid surface charge patterns (Supplementary Section V). Therefore, we emphasize that in order to rigorously assess the role of electrostatic interactions on chiral nematic ordering, one should carefully consider the variations of the cholesteric pitch at different pH and ionic conditions as a function of the reduced density C/C_{iso}, so as to accurately distinguish the potential contributions attributable to the chiral charge distribution from those arising from the generic effects of electrostatic forces on the nematic stability range. This task is likely arduous in cholesteric phases of fibrous biomaterials lacking a well-resolved, monodisperse morphology, for which the determination of C_{iso} is necessarily ambiguous—thus hindering the unequivocal experimental characterization of these distinct steric and electrostatic chirality transfer mechanisms in such cases. However, another experimental signature of the steric-based suprahelix model lies in the tightening of the cholesteric pitch with increasing particle contour length L_c (Supplementary Section VII), which contradicts classical theoretical predictions for screw-like particles[47] and rod-shaped particles featuring helical surface charges[40]. Interestingly, a similar behaviour has been recently reported in fractionated cellulose[20] as well as in amyloid fibril suspensions[17], which suggests that such excluded-volume-driven modes of chirality propagation may find broader potential applications within a wider class of experimental colloidal and biological liquid crystalline systems. Overall, our findings emphasize how chirality transfer may arise from subtle chiral contributions of opposite handedness, which, depending on their magnitude and sign, can act either synergistically or competitively, therefore resulting in the diversity of chiral phase behaviours observed in nearly identical systems.

By combining both mesoscopic experimental measurements and theoretical predictions based on first-principles atomistic models, our work further provides a general methodological framework for the bottom-up, quantitative description of chirality transfer across length scales in cholesteric liquid crystals. Understanding and controlling how chirality is expressed and transmitted in such helical superstructures not only may shed light on the various self-assembly processes and mechanisms leading to the large diversity of chiral liquid crystalline organizations, but also holds promise for the design of novel chiral materials with tailored optical, electronic or biological functionalities[4–6].

Online content

Any methods, additional references, Nature Portfolio reporting summaries, source data, extended data, supplementary information, acknowledgements, peer review information; details of author contributions and competing interests; and statements of data and code availability are available at https://doi.org/10.1038/s41563-024-01897-x.

References

1. Liu, M., Zhang, L. & Wang, T. Supramolecular chirality in self-assembled systems. *Chem. Rev.* **115**, 7304–7397 (2015).

2. Morrow, S. M., Bissette, A. J. & Fletcher, S. P. Transmission of chirality through space and across length scales. *Nat. Nanotechnol.* **12**, 410–419 (2017).
3. Nemati, A. et al. Chirality amplification by desymmetrization of chiral ligand-capped nanoparticles to nanorods quantified in soft condensed matter. *Nat. Commun.* **9**, 3908 (2018).
4. Zhang, X. et al. Liquid crystal-templated chiral nanomaterials: from chiral plasmonics to circularly polarized luminescence. *Light Sci. Appl.* **11**, 223 (2022).
5. Sang, Y. & Liu, M. Hierarchical self-assembly into chiral nanostructures. *Chem. Sci.* **13**, 633–656 (2022).
6. Kotov, N. A., Liz-Marzán, L. M. & Wang, Q. Chiral nanomaterials: evolving rapidly from concepts to applications. *Mater. Adv.* **3**, 3677–3679 (2022).
7. Mitov, M. Cholesteric liquid crystals with a broad light reflection band. *Adv. Mater.* **24**, 6260–6276 (2012).
8. Bisoyi, H. K. & Li, Q. Liquid crystals: versatile self-organized smart soft materials. *Chem. Rev.* **122**, 4887–4926 (2022).
9. Mitov, M. Cholesteric liquid crystals in living matter. *Soft Matter* **13**, 4176–4209 (2017).
10. Reinitzer, F. Beiträge zur kenntniss des cholesterins. *Monatshefte Chem.* **9**, 421–441 (1888).
11. Livolant, F. & Leforestier, A. Condensed phases of DNA: structures and phase transitions. *Prog. Polym. Sci.* **21**, 1115–1164 (1996).
12. Zanchetta, G. et al. Right-handed double-helix ultrashort DNA yields chiral nematic phases with both right- and left-handed director twist. *Proc. Natl Acad. Sci. USA* **107**, 17497–17502 (2010).
13. Siavashpouri, M. et al. Molecular engineering of chiral colloidal liquid crystals using DNA origami. *Nat. Mater.* **16**, 849–856 (2017).
14. Dogic, Z. & Fraden, S. Cholesteric phase in virus suspensions. *Langmuir* **16**, 7820–7824 (2000).
15. Grelet, E. & Fraden, S. What is the origin of chirality in the cholesteric phase of virus suspensions? *Phys. Rev. Lett.* **90**, 198302 (2003).
16. Tombolato, F., Ferrarini, A. & Grelet, E. Chiral nematic phase of suspensions of rodlike viruses: left-handed phase helicity from a right-handed molecular helix. *Phys. Rev. Lett.* **96**, 258302 (2006).
17. Bagnani, M., Nyström, G., De Michele, C. & Mezzenga, R. Amyloid fibrils length controls shape and structure of nematic and cholesteric tactoids. *ACS Nano* **13**, 591–600 (2019).
18. Belamie, E., Davidson, P. & Giraud-Guille, M. M. Structure and chirality of the nematic phase in α-chitin suspensions. *J. Phys. Chem. B* **108**, 14991–15000 (2004).
19. Araki, J. & Kuga, S. Effect of trace electrolyte on liquid crystal type of cellulose microcrystals. *Langmuir* **17**, 4493–4496 (2001).
20. Honorato-Rios, C. & Lagerwall, J. P. F. Interrogating helical nanorod self-assembly with fractionated cellulose nanocrystal suspensions. *Commun. Mater.* **1**, 69 (2020).
21. Parton, T. G. et al. Chiral self-assembly of cellulose nanocrystals is driven by crystallite bundles. *Nat. Commun.* **13**, 2657 (2022).
22. Straley, J. P. Theory of piezoelectricity in nematic liquid crystals, and of the cholesteric ordering. *Phys. Rev. A* **14**, 1835–1841 (1976).
23. Harris, A. B., Kamien, R. D. & Lubensky, T. C. Molecular chirality and chiral parameters. *Rev. Mod. Phys.* **71**, 1745–1757 (1999).
24. Osipov, M. A. Theory for cholesteric ordering in lyotropic liquid crystals. *Nuovo Cim. D* **10**, 1249–1262 (1988).
25. Cherstvy, A. G. DNA cholesteric phases: the role of DNA molecular chirality and DNA electrostatic interactions. *J. Phys. Chem. B* **142**, 12585–12595 (2008).
26. Dussi, S. & Dijkstra, M. Entropy-driven formation of chiral nematic phases by computer simulations. *Nat. Commun.* **7**, 11175 (2016).
27. Tortora, M. M. C., Mishra, G., Prešern, D. & Doye, J. P. K. Chiral shape fluctuations and the origin of chirality in cholesteric phases of dna origamis. *Sci. Adv.* **6**, eaaw8331 (2020).
28. Dogic, Z. & Fraden, S. *Soft Matter* Vol. 2 (eds Gompper, G. & Schick, M.) (Wiley-VCH, 2006).
29. Smith, G. P. & Petrenko, V. A. Phage display. *Chem. Rev.* **97**, 391–410 (1997).
30. Marvin, D. A., Welsh, L. C., Symmons, M. F., Scott, W. R. P. & Straus, S. K. Molecular structure of fd (f1, M13) filamentous bacteriophage refined with respect to X-ray fibre diffraction and solid-state NMR data supports specific models of phage assembly at the bacterial membrane. *J. Mol. Biol.* **355**, 294–309 (2006).
31. Lee, Y. J. et al. Fabricating genetically engineered high-power lithium-ion batteries using multiple virus genes. *Science* **324**, 1051–1055 (2009).
32. Marvin, D. A., Symmons, M. F. & Straus, S. K. Structure and assembly of filamentous bacteriophages. *Prog. Biophys. Mol. Biol.* **114**, 80–122 (2014).
33. Gibaud, T. et al. Self-assembly through chiral control of interfacial tension. *Nature* **481**, 348–351 (2012).
34. Grelet, E. Hard-rod behavior in dense mesophases of semiflexible and rigid charged viruses. *Phys. Rev. X* **4**, 021053 (2014).
35. Willis, B. et al. Biologically templated organic polymers with nanoscale order. *Proc. Natl Acad. Sci. USA* **105**, 1416–1419 (2008).
36. Chung, W.-J. et al. Biomimetic self-templating supramolecular structures. *Nature* **478**, 364–368 (2011).
37. Barry, E. & Dogic, Z. A model liquid crystalline system based on rodlike viruses with variable chirality and persistence length. *Soft Matter* **5**, 2563–2570 (2009).
38. Frezza, E., Ferrarini, A., Bindu Kolli, H., Giacometti, A. & Cinacchi, G. Left or right cholesterics? A matter of helix handedness and curliness. *Phys. Chem. Chem. Phys.* **16**, 16225–16232 (2014).
39. Dussi, S., Belli, S., van Roij, R. & Dijkstra, M. Cholesterics of colloidal helices: predicting the macroscopic pitch from the particle shape and thermodynamic state. *J. Chem. Phys.* **142**, 074905 (2015).
40. Kornyshev, A. A., Leikin, S. & Malinin, S. V. Chiral electrostatic interaction and cholesteric liquid crystals of DNA. *Eur. Phys. J. E* **7**, 83–93 (2002).
41. Wensink, H. H. & Jackson, G. Generalized van der Waals theory for the twist elastic modulus and helical pitch of cholesterics. *J. Chem. Phys.* **130**, 234911 (2009).
42. Zhang, C., Diorio, N., Lavrentovich, O. D. & Jákli, A. Helical nanofilaments of bent-core liquid crystals with a second twist. *Nat. Commun.* **5**, 3302 (2014).
43. Oostenbrink, C., Villa, A., Mark, A. E. & Van Gunsteren, W. F. A biomolecular force field based on the free enthalpy of hydration and solvation: the GROMOS force-field parameter sets 53A5 and 53A6. *J. Comput. Chem.* **25**, 1656–1676 (2004).
44. Grelet, E. & Rana, R. From soft to hard rod behavior in liquid crystalline suspensions of sterically stabilized colloidal filamentous particles. *Soft Matter* **12**, 4621–4627 (2016).
45. Tang, J. & Fraden, S. Isotropic-cholesteric phase transition in colloidal suspensions of filamentous bacteriophage *fd*. *Liq. Cryst.* **19**, 459–467 (1995).
46. Narkevicius, A. et al. Controlling the self-assembly behavior of aqueous chitin nanocrystal suspensions. *Biomacromolecules* **20**, 2830–2838 (2019).
47. Odijk, T. Pitch of a polymer cholesteric. *J. Phys. Chem.* **91**, 6060–6062 (1987).
48. Jurrus, E. et al. Improvements to the APBS biomolecular solvation software suite. *Protein Sci.* **27**, 112–128 (2018).
49. Chen, Z. Y. Nematic ordering in semiflexible polymer chains. *Macromolecules* **26**, 3419–3423 (1993).

Methods

Virus strains and capsid symmetries

For this study, we employ two strains of filamentous bacteriophages referred to as M13 and Y21M (refs. 30,32). Both viruses belong to the Ff phage family, which includes the fd virus, and infect male (F^+) *Escherichia coli* (*E. coli*). The phage capsid, protecting a single-stranded circular DNA core, is primarily composed of about 3,000 copies of 50-residue, identical α-helical subunits, called p8 proteins, assembled into an overlapping, interdigitated helical structure. M13 and Y21M bear a high genetic similarity to the fd strain, implying that structural and biological properties are strongly conserved across these virions. In details, M13 and fd differ only by a single amino acid mutation at position 12 of the major coat protein p8, whereby a negatively charged aspartate (Asp) in fd is substituted by a neutral asparagine (Asn) in M13. This change in the solvent-accessible section of the protein modifies its overall charge but does not structurally affect the symmetry of the two viruses. Indeed, both virions have been shown to have an identical capsid structure, as determined by X-ray fibre diffraction and NMR studies, deposited under the 1IFI model in the PDB[30,50]. Conversely, for Y21M, the single amino acid mutation occurs deeper within the capsid at position 21 in the coat proteins p8, where a tyrosine (Tyr) in M13 and fd is replaced by a methionine (Met) in Y21M. This substitution alters the symmetry of the phage capsid and leads to a five-fold rotation axis combined with an exact two-fold helical axis (C_5S_2 symmetry), associated with a precise rotation angle of 36° between two consecutive pentameric rings of p8 proteins—as described in the 2C0W model in the PDB. This contrasts with the 1IFI model of M13, for which this angle is measured to be 33.23°, corresponding to a slight deviation from the two-fold screw symmetry[32]. Another difference between the two strains concerns the axial distance between two consecutive pentameric subunits, varying from 1.60 to 1.67 nm depending on the model (Fig. 1)[30,50]. As a consequence of the spatial arrangement of the major coat proteins, a main geometrical groove as deep as 1 nm (ref. 51) exists on both phage capsids, corresponding to a right-handed thread characterized by the angle $\varphi = 39.85°$ for M13 and 43.15° for Y21M (Figs. 1 and 2). A second right-handed thread can be identified on the M13 capsid, resulting from the lack of exact C_5S_2 symmetry in the 1IFI model and characterized by the angle $\psi = 5.15°$, whereas this groove is achiral for Y21M (2C0W model) with $\psi = 0°$ (Fig. 1). These subtle structural differences between the two phages result in a large change of one of their physical properties, that is, their stiffness, with a persistence length of $L_p = 9.9$ µm for Y21M that contrasts with $L_p = 2.8$ µm for the semi-flexible M13 strain[37]. Conversely, their contour lengths L_c measured by transmission electron microscopy[52] are very close with $L_c = 995$ nm and 920 nm for M13 and Y21M, respectively, and both viruses have the same diameter of about $d = 7$ nm (Fig. 1). The major coat proteins, p8, provide both viruses with a helical charge distribution and a negative surface charge in physiological conditions, carried by ionic amino acids exposed to the aqueous solvent. This net charge decreases as the buffer pH approaches the isoelectric point pI_E (Fig. 2), which is in the range 4.2–4.5 for Y21M and M13 (ref. 53).

Virus preparation

Both M13 and Y21M viruses are grown using the ER2738 strain as the *E. coli* host bacteria and purified following standard biological protocols. Virus PEGylation is performed by covalent binding between coat protein amino groups and *N*-hydroxysuccinimide ester-activated PEG of average molecular weight 21 kg mol^{-1} and radius of gyration $R_g \approx 7$ nm, as described in more detail in ref. 44. PEGylation results in about 330 PEG chains per virus, and the associated phase behaviour is shown to be driven by steric repulsion, that is, to be independent of ionic strength[44]. Note that the isoelectric point and persistence length of PEGylated viruses are expected to be similar to those of unmodified viruses, as only a limited fraction of about 10% of the coat proteins are bound with PEG[54]. By neglecting the curvature of the virion capsid, this coverage with PEG polymers yields an upper-bound estimate for the surface lateral pressure $\Pi \approx 0.1$ mN m^{-1} (refs. 54,55), associated with a total effective force $F \propto \Pi/R_g \times dL_c \approx 10$ pN exerted onto the capsid—more than two orders of magnitude below the typical elastic stretching modulus reported for such filamentous viruses[56]. The virus concentration C_{virus} at each dilution level is determined using spectrophotometry[37] with an error bar of ±2 mg ml^{-1}. For PEGylated viruses, the volume fraction Φ is calculated using an effective rod diameter $d_{eff} = d + 4R_g$ according to the following: $\Phi = \frac{C_{virus}N_A}{M_w} \times \frac{\pi}{4} L_c d_{eff}^2$, where M_w is the virus molecular weight and N_A is Avogadro's number[44]. In order to study the pH dependence of the cholesteric pitch, different biological buffers are used covering basic to acidic conditions: 2-(cyclohexylamino) ethanesulfonic acid (pK_a 9.3); (tris(hydroxymethyl)aminomethane (pK_a 8.2); 4-morpholineethanesulfonic acid (pK_a 6.1); pyridine (pK_a 5.2); propianic acid (pK_a 4.9); acetic acid (pK_a 4.7); and chloroacetic acid (pK_a 2.9). The buffering agent is introduced with an analytical concentration of 20 mM, and pH and ionic strength I_S are adjusted with tunable amounts of NaOH (or HCl) and NaCl, respectively. After extensive dialysis, virus suspensions of different dilutions are prepared in previously cleaned (successive rinsing with acetone, isopropanol and distilled water followed by 30 min of UV–ozone treatment (Harrick Plasma)) quartz capillary tubes of diameter ~1.5 mm for polarizing microscopy observations, and between a cover slip and glass slide with a parafilm spacer of about 100 µm for samples used for handedness determination by fluorescence microscopy. In the latter case, samples are doped at a fraction of 1:10^5 with red- or green-labelled viruses, grafted with DyLight 550 *N*-hydroxysuccinimide ester (Thermo Fischer) and Alexa Fluor 488 *N*-hydroxysuccinimide ester (Thermo Fischer), respectively.

Optical microscopy experiments

Epifluorescence images are obtained using an inverted optical microscope (IX71, Olympus) equipped with a ×100 oil-immersion objective (numerical aperture, 1.4; UPLSAPO); a piezo device for objective *z*-positioning (P-721 PIFOC Piezo Flexure Objective Scanner, PI) operated by computer interface software (Meta-Morph, Molecular Devices); a light-emitting diode (LED) light engine (LedHUB, Omicron); and a fluorescence imaging camera (Neo sCMOS, Andor Technology). The mirror symmetry of the whole optical set-up is checked before each observation. The kinetics of establishing the chiral nematic phase is shown to be sample dependent: a few days to a few weeks of equilibration are applied to get homogeneous fingerprint textures (inset of Fig. 3 and Extended Data Fig. 4f), resulting from the virion planar anchoring at the capillary walls. Cholesteric pitch measurements are carried out at low magnification (×5 LMPlanFl objective; numerical aperture, 0.13) with a polarizing microscope (BX-51, Olympus) equipped with a JAI-CV-M7+ colour camera. The cholesteric pitch determined from fingerprint textures is an average value of 10 to 20 measurements, and error bars correspond to the dispersion of the experimental values. The nematic phase is ascribed to samples for which no helical pitch is observed over the millimetre range, corresponding to the capillary diameter.

Numerical methods

The molecular structures of the whole capsids of the M13 and Y21M viruses are respectively reconstructed from the atomic models 1IFI and 2C0W deposited in the PDB (as described previously)[30,50]. Potential energies are parametrized using the GROMOS 53A6 force field[43] to explicitly account for van der Waals and excluded-volume interactions between each pair of atoms within the capsids. Screened electrostatic contributions are described by the generalized reaction field method[57], corresponding to a computationally efficient treatment of long-ranged electrostatic forces based on the Kirkwood–Onsager continuum theory of dielectric polarization[57]. In particular, this approach allows for the use of a finite truncation cut-off (as described in the following),

combined with an implicit representation of the ionic environment in terms of the solvent ionic strength, temperature and dielectric permittivity; it has been shown to accurately capture the thermodynamics of a wide variety of protein condensates[43]. Molecular charge distributions are determined using the PROPKA plugin of the pdb2pqr pipeline[58]. For computational tractability, a cut-off radius $r_{cut} = 3.5$ nm is applied in the calculation of all electrostatic energies. This approximation is expected to hold in the limit where the Debye screening length κ^{-1} is such that $\kappa^{-1} \ll r_{cut}$, which is typically valid for ionic strengths $I_S \geq 100$ mM. In this context, the effective steric contribution is computed by evaluating the full force field in the limit of very high salt concentrations ($I_S = 1$ M).

For the computation of cholesteric pitches, the system free energy $\mathcal{F}$ is derived for both the electrostatic and suprahelix models at the second virial level as a functional of the full intermolecular pairwise potential U_{inter}, based on a perturbative expansion of the Onsager expression $\mathcal{F}_0$ for the uniform, untwisted nematic state (Supplementary Section I). The optimal angular arrangement of the particles about the local director, which generally depends on the detailed virus structure and thermodynamic state, is determined by functional minimization of $\mathcal{F}_0$ at fixed concentration[27]. The corresponding equilibrium pitch P and the twist elastic constant K_{22} are obtained by subsequent minimization of the full free energy $\mathcal{F}$ based on the computed local orientational distribution (Supplementary Section I), and may be formulated in terms of a hierarchy of generalized virial integrals involving U_{inter} (ref. 27). Such integrals are evaluated via high-performance Monte Carlo sampling techniques as described elsewhere[59]. Importantly, this framework enables us to accurately infer the most favourable, large-scale (micro- to millimetre range) cholesteric structure from the atomistic details of the different virus models, with a level of precision tunable through the statistical resolution of the stochastic integration scheme[27]. Accordingly, error bars are estimated as the standard error of the computed pitches across ten independent Monte Carlo runs, using a number $\approx 10^{14}$ of integration steps. Binodal points are calculated by equating chemical potentials and osmotic pressures in the isotropic and cholesteric phases, and solving the resulting coupled coexistence equations numerically[27].

Data availability

All the data supporting the findings of this study are included in the article and its Supplementary Information file. Source data are provided with this paper.

Code availability

The numerical codes used for molecular structure preparation and density functional calculations can be accessed via GitHub at https://github.com/mtortora/chiralDFT.

References

50. Morag, O., Sgourakis, N. G., Baker, D. & Goldbourt, A. The NMR-Rosetta capsid model of M13 bacteriophage reveals a quadrupled hydrophobic packing epitope. *Proc. Natl Acad. Sci. USA* **112**, 971–976 (2015).
51. Kishchenko, G., Batliwala, H. & Makowski, L. Structure of a foreign peptide displayed on the surface of bacteriophage M13. *J. Mol. Biol.* **241**, 208–213 (1994).
52. Pouget, E., Grelet, E. & Lettinga, M. P. Dynamics in the smectic phase of stiff viral rods. *Phys. Rev. E Stat. Nonlinear Soft Matter Phys.* **84**, 041704 (2011).
53. Zimmermann, K., Hagedorn, H., Heucks, C. C., Hinrichsen, M. & Ludwig, H. The ionic properties of the filamentous bacteriophages Pfl and fd. *J. Biol. Chem.* **261**, 1653–1655 (1986).
54. Zan, T. et al. Into the polymer brush regime through the "grafting-to" method: densely polymer-grafted rodlike viruses with an unusual nematic liquid crystal behavior. *Soft Matter* **12**, 798–805 (2016).
55. Marsh, D. Elastic constants of polymer-grafted lipid membranes. *Biophys. J.* **81**, 2154–2162 (2001).
56. Khalil, A. S. et al. Single M13 bacteriophage tethering and stretching. *Proc. Natl Acad. Sci. USA* **104**, 4892–4897 (2007).
57. Tironi, I. G., Sperb, R., Smith, P. E. & van Gunsteren, W. F. A generalized reaction field method for molecular dynamics simulations. *J. Chem. Phys.* **102**, 5451–5459 (1995).
58. Olsson, M. H. M., Søndergaard, C. R., Rostkowski, M. & Jensen, J. H. PROPKA3: consistent treatment of internal and surface residues in empirical pK_a predictions. *J. Chem. Theory Comput.* **7**, 525–537 (2011).
59. Tortora, M. M. C. & Doye, J. P. K. Hierarchical bounding structures for efficient virial computations: towards a realistic molecular description of cholesterics. *J. Chem. Phys.* **147**, 224504 (2017).

Acknowledgements

We thank H. Anop for the data of Extended Data Fig. 5 and A. Pope for help with Y21M sample preparation. We also acknowledge access to computing resources provided by the Pôle Scientifique de Modélisation Numérique of the ENS de Lyon.

Author contributions

E.G. conceptualized the study, instigated the project, performed the experiments and wrote the paper with contributions from M.M.C.T.; M.M.C.T. implemented the numerical methods and carried out the calculations. Both authors developed the models, analysed the results, wrote the Supplementary Information and revised and edited the paper. Correspondence and requests for materials and data should be addressed to E.G. Queries regarding numerical details and computational data should be directed to M.M.C.T.

Competing interests

The authors declare no competing interests.

Additional information

Extended data is available for this paper at https://doi.org/10.1038/s41563-024-01897-x.

Supplementary information The online version contains supplementary material available at https://doi.org/10.1038/s41563-024-01897-x.

Correspondence and requests for materials should be addressed to Eric Grelet or Maxime M. C. Tortora.

Peer review information *Nature Materials* thanks Torsten Hegmann, Jan Lagerwall and the other, anonymous, reviewer(s) for their contribution to the peer review of this work.

https://doi.org/10.1038/s41563-024-01897-x

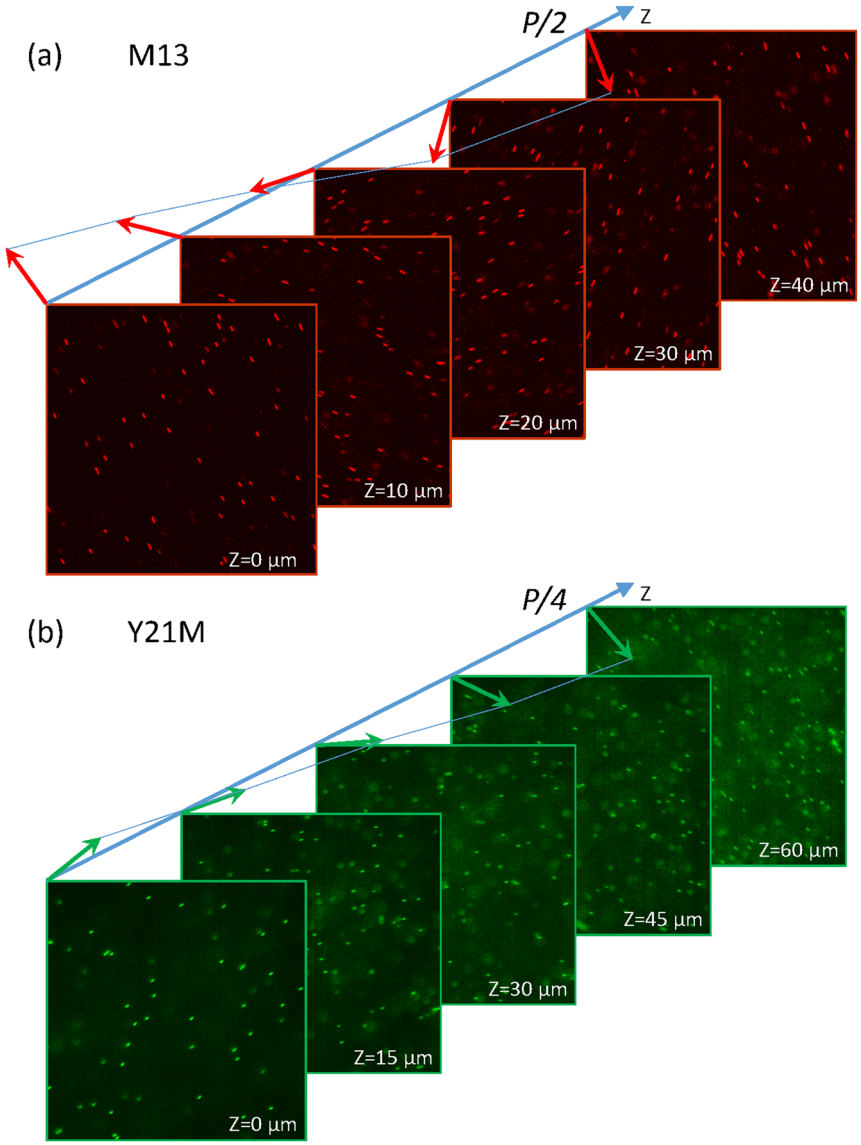

Extended Data Fig. 1 | Opposite handedness of the cholesteric helix for M13 and Y21M strains. Determined by fluorescence microscopy in (a) PEGylated M13 suspension (pH 8.2, I_S=110 mM) and (b) Y21M suspension (pH 8.2, I_S=60 mM). A small fraction (1:10^5) of viruses are labelled with red or green fluorescent tags to indicate the orientation of the nematic director in each focal plane, as shown by arrows. Their rotation through the sample thickness Z reveals the handedness of the cholesteric helicity, which is found to be left-handed for M13 and M13-PEG and right-handed for Y21M strain. The periodicity of the cholesteric helix, or cholesteric pitch *P*, is also indicated for both virion strains, and its value is positive (negative) for right (left) handedness. Each image has a size of 50 μm x 50 μm.

https://doi.org/10.1038/s41563-024-01897-x

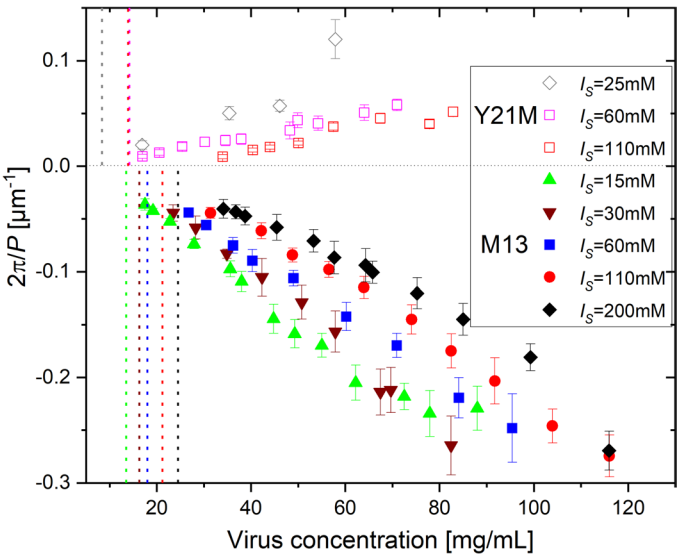

Extended Data Fig. 2 | Electrostatic dependence of the cholesteric pitch, *P*. Measurements for Y21M (open symbols) and M13 (full symbols) for different ionic strengths I_S at fixed pH 8 as a function of the respective virus concentration. The data of Y21M phages at pH 8 and I_S = 110 mM are taken from Ref. 37. For both virions, $|P|$ increases with increasing ionic strength, that is, with increasing the screening of electrostatic interactions. For each data set, the binodal concentrations of the isotropic-to-cholesteric transition corresponding to the stability limit of the isotropic phase, C_{iso}, are shown by a dotted line whose colour corresponds to the associated colour of the symbols. For error bar determination, see Methods.

https://doi.org/10.1038/s41563-024-01897-x

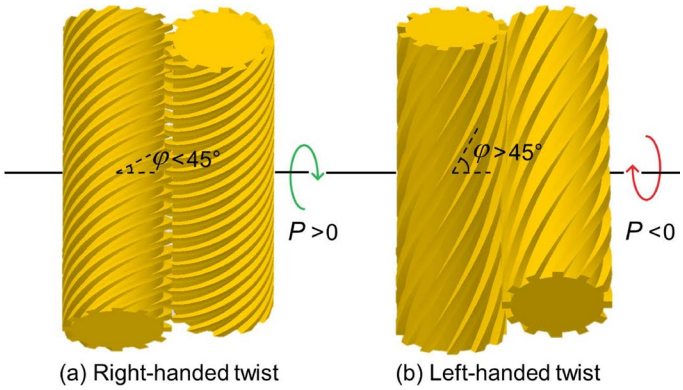

Extended Data Fig. 3 | Inversion of the twist handedness between right-handed screws of varying thread angle, φ. The helical twist resulting from the close packing of two *right*-handed (that is $0 < \varphi < +90°$) screws leads (a) to a *right*-handed twist (and therefore a right-handed cholesteric pitch $P > 0$) of angle $2\varphi > 0$ when $\varphi < 45°$ and (b) to a *left*-handed twist ($P < 0$) of angle $-(180° - 2\varphi) < 0$ for $\varphi > 45°$.

https://doi.org/10.1038/s41563-024-01897-x

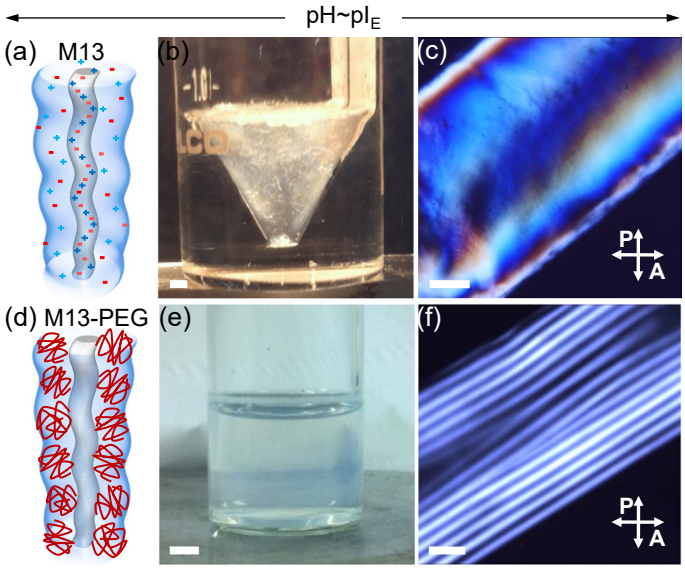

Extended Data Fig. 4 | Phase behaviour of semi-flexible M13 (a)-(c) and PEGylated M13-PEG (d)-(f) virus suspensions at pH close to the isoelectric point, pI$_E$. (a) and (d): Schematic representation of the filamentous viruses, whose colloidal stability stems from either (a) electrostatic or (d) steric repulsion. (b) and (e): Macroscopic observation under white light of the virion suspensions: while aggregates are observed in raw M13 virus dispersions at pH ≃ pI$_E$, the colloidal stability is preserved in the M13-PEG system. Scale bar: 2 mm. (c) and (f): Polarized optical microscopy images displaying a nematic-like birefingent texture with fibrillar moieties for raw M13 viruses (c) and the characteristic fingerprint texture of the cholesteric phase for PEGylated particles (f). Scale bar: 200 μm.

https://doi.org/10.1038/s41563-024-01897-x

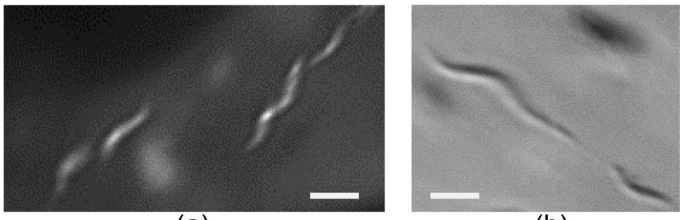

Extended Data Fig. 5 | Helical supramolecular structures. They are formed by condensation of filamentous viruses initially organized in a cholesteric mesophase, induced by depletion interaction using poly(ethylene glycol) polymer (molecular weight M_w=2000 g mol^{-1}; Sigma-Aldrich) and observed by (a) polarizing and (b) differential interference contrast (DIC) microscopy. Scale bar: 2 μm.

nature materials

Supplementary information

https://doi.org/10.1038/s41563-024-01897-x

Elucidating chirality transfer in liquid crystals of viruses

In the format provided by the authors and unedited

CONTENTS

I. FRANK-OSEEN FREE ENERGY OF THE CHOLESTERIC STATE

According to the continuum elastic theory of the nematic liquid crystalline state, the Frank-Oseen free energy density f can be expanded in a power series of the twist deformation of the orientational ordering: $f \approx f_0 + K_t q + \frac{1}{2} K_{22} q^2$, where f_0 is the free energy density of the undeformed nematic phase [1] and q accounts for the deformation wavelength. The inverse cholesteric pitch $q = 2\pi/P$ is obtained by minimizing the free energy: $q = -K_t/K_{22}$, with $K_t = (\partial f/\partial q)_{q=0}$ the chiral strength and $K_{22} = (\partial^2 f/\partial q^2)_{q=0}$ the twist elastic constant [2, 3]. K_t accounts for the intrinsic propensity of the system to generate twist deformations, as a consequence of chirality of the intermolecular interactions; K_t changes its sign for chiral enantiomers, and vanishes in the absence of molecular chirality. K_{22} is the twist elastic constants and accounts for the resistance of the liquid crystal order to orientational deformation (see Section II).

Let us consider a cholesteric phase of director field $\mathbf{n}$ and helical axis $\mathbf{e}_z$ in the laboratory frame $\mathcal{R}_{\rm lab} \equiv \big[\mathbf{e}_x \ \mathbf{e}_y \ \mathbf{e}_z\big]$. In the absence of macroscopic twist ($q \to 0$), the free energy density f_0 of the reference nematic state with uniform director $\mathbf{n}_0 \equiv \mathbf{e}_x$ reads as, at the second-virial level [3, 4],

$$\beta f_0[\psi] = 4\pi^2 \rho \int_{-1}^{1} du_x \, \psi(u_x) \Big\{ \log\big[\rho \lambda^3 \psi(u_x)\big] - 1 \Big\} - \frac{\rho^2}{2} \int_V d\mathbf{r}_{12} \oiint d\mathcal{R}_1 d\mathcal{R}_2 \, \psi(u_{1x}) \psi(u_{2x}) f(\mathbf{r}_{12}, \mathcal{R}_1, \mathcal{R}_2), \quad (1)$$

where the Mayer function f depends on the full atomistic interaction energy $U_{\rm inter}$ of a pair of viruses with respective orientations $\mathcal{R}_{1,2}$ and relative center-of-mass separation $\mathbf{r}_{12}$,

$$f(\mathbf{r}_{12}, \mathcal{R}_1, \mathcal{R}_2) \equiv \exp\big\{ -\beta U_{\rm inter}(\mathbf{r}_{12}, \mathcal{R}_1, \mathcal{R}_2) \big\} - 1,$$

with $\beta \equiv 1/k_B T$. In Eq. (1), ψ is the so-called orientational distribution function, which quantifies the angular fluctuations of the virus long axes $\mathbf{u} \equiv \mathcal{R} \cdot \mathbf{e}_x$ about $\mathbf{n}_0$, and $\lambda \equiv \lambda(T)$ is an irrelevant (de Broglie) thermal lengthscale.

At thermodynamic equilibrium, the most-favorable particle arrangement corresponds to the optimal degree of local nematic alignment of the viruses, as described by the dispersion of angles $\cos\theta \equiv \mathbf{u} \cdot \mathbf{n}_0$, and may be obtained by functional minimization of Eq. (1) at fixed temperature T and virus number density ρ,

$$\psi_{\rm eq}(\cos\theta) = \frac{1}{Z} \exp\left\{ \frac{\rho}{4\pi^2} \int_V d\mathbf{r}_{12} \oiint d\mathcal{R}_1 d\mathcal{R}_2 \, \psi_{\rm eq}(u_{2x}) f(\mathbf{r}_{12}, \mathcal{R}_1, \mathcal{R}_2) \times \delta\big(u_{1x} - \cos\theta\big) \right\}, \quad (2)$$

where δ is the Dirac distribution and Z a Lagrange multiplier ensuring the proper normalization of Eq. (2) [3]. K_{22} and K_t may then be derived in the form [5]

$$\beta K_{22} = \frac{\rho^2}{2} \int_V d\mathbf{r}_{12} \oiint d\mathcal{R}_1 d\mathcal{R}_2 \, f(\mathbf{r}_{12}, \mathcal{R}_1, \mathcal{R}_2) \times \dot{\psi}_{\mathrm{eq}}(u_{1x}) \dot{\psi}_{\mathrm{eq}}(u_{2x}) r_z^2 u_{1y} u_{2y}, \tag{3}$$

$$\beta K_t = -\frac{\rho^2}{2} \int_V d\mathbf{r}_{12} \oiint d\mathcal{R}_1 d\mathcal{R}_2 \, f(\mathbf{r}_{12}, \mathcal{R}_1, \mathcal{R}_2) \times \psi_{\mathrm{eq}}(u_{1x}) \dot{\psi}_{\mathrm{eq}}(u_{2x}) r_z u_{2y}, \tag{4}$$

with $\dot{\psi}_{\mathrm{eq}}$ the first derivative of ψ_{eq}. Eq. (2) is solved numerically via a self-consistent iterative algorithm [6], and Eqs. (3)–(4) are evaluated using accurate and optimized virial integration schemes [7], as discussed in detail elsewhere [3, 8]. The corresponding numerical codes are available on GitHub [9].

II. TWIST ELASTIC CONSTANT K_{22}

The twist elastic constant K_{22}, as introduced in the Frank-Oseen free energy for the nematic elasticity (see Section I), describes the resistance of the liquid crystal to helical deformation [1]. While elastic constants have been measured for various molecular mesophases, experimental values for colloidal liquid crystals are rather scarce to date [10, 11]. Here, we compare experimental and theoretical values for K_{22}, with the later calculated by minimizing the free energy density of the electrostatic model (2C0W), as well as the suprahelix one (Fig. S1). After renormalization of the virus concentration by their respective binodal concentration C_{iso}, it turns out that K_{22} is almost independent of the different probed parameters, i.e. the atomistic details of the virion surface (charge distributions), the electrostatic interactions (pH and ionic strength), and the overall particle shape (backbone helicity). The nearly linear concentration dependence of K_{22} is not observed in reported experimental data for semi-flexible viruses, rather a constant value of about $K_{22} \simeq 100 k_B T/\mu m$ is found [10]. As data are missing for rigid filamentous viruses, we measure experimentally the twist elastic constant for stiff Y21M phages by unwinding its cholesteric phase under external magnetic field [1]. Specifically, K_{22} is obtained by determining the critical magnetic field H_c necessary to induce the cholesteric-to-nematic phase transition, which are related by [1]:

$$K_{22} = \chi_v \left(\frac{P \times H_c}{\pi^2} \right)^2, \tag{5}$$

where P is the cholesteric pitch in absence of magnetic field, and χ_v the diamagnetic anisotropy per unit volume. χ_v depends on the diamagnetic anisotropy $\chi_0 = \chi_\parallel - \chi_\perp =$

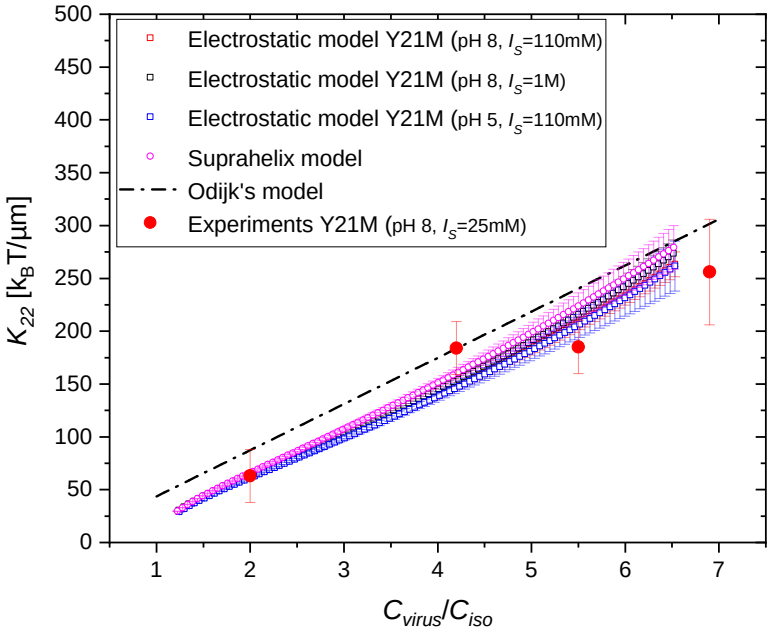

FIG. S1. **Twist elastic constant**, K_{22}, as a function of the normalized viral rod concentration calculated with electrostatic (2C0W) and suprahelix models (open symbols) at three different ionic conditions, and measured experimentally for stiff Y21M phages (full red dots, I_S=25 mM). Our theoretical and experimental results are in very good agreement, and are consistent with the analytical expression of K_{22} obtained by Odijk [12] for rigid hard rods (Eq. (7), black dashed line). Error bars are determined as detailed in Methods.

7×10^{-24} J/T^2 per virus particle [10], via $\chi_v = \rho\chi_0$ with $\rho = C_{virus}N_A/M_W$ the rod number density, $M_W = 1.64 \times 10^7$ g/mol the virus molecular weight, and N_A Avogadro's number.

Experiments are performed using an home made electro-magnet with a gap of about 6 cm between the magnet poles of diameter 9.5 cm, allowing for an uniform field to be applied to capillary samples. The resulting magnetic field can be finely tuned by varying the current up to 36 A corresponding to maximal magnetic field of H_{max}=1.10 T. The critical magnetic field H_c to induce the cholesteric-to-nematic transition is determined by incremental increases of the magnetic field. Each field increment $\Delta H = 0.05$ to 0.1 T is applied for about 1 hour to allow for sample stabilization, followed by a quick sample observation with optical polarizing microscopy. The resulting twist elastic constants (Eq. 5) are shown in Fig. S1. Experimental values of K_{22} are in very good agreement with the theoretical ones, and differ significantly by their linear dependence with the particle concentration from the results reported for

semi-flexible bacteriophages [10]. It is worth pointing out that the linear increase of K_{22} with the particle volume fraction is consistent with Odijk's theory [12] (Fig. S1). Indeed, theoretical predictions by Odijk represent a benchmark for the Frank-Oseen elastic constant determination of long stiff hard rods, for which an analytical expression of K_{22} has been derived in the limit of strong orientational alignment and within the range of validity of the second virial approximation [12]:

$$K_{22} = \frac{7}{24\pi}\frac{k_B T}{d}\Phi\frac{L_c}{d}. \tag{6}$$

By substituting in Eq. 6 the binodal value predicted by Onsager's theory for high rod aspect ratio, $\Phi_{iso} \simeq 3.3\frac{d}{L_c}$, we obtain:

$$K_{22} \simeq 0.3\frac{k_B T}{d}\frac{\Phi}{\Phi_{iso}}, \tag{7}$$

as plotted in Fig. S1.

It is worth emphasizing that the determination of the twist elastic constant is of major importance when studying the experimental dependence of the cholesteric pitch P, defined as $P = 2\pi K_{22}/K_t$ (see Supplementary Section I). Indeed, for a given system, any variation of the pitch cannot be unequivocally attributed to the variation of the chiral strength K_t, but may be significantly affected by a change of the twist elastic constant K_{22}, as it may occur for instance close to a phase transition.

III. ELECTROSTATIC MODEL VS. SEMI-FLEXIBLE M13 VIRUS STRAIN

In Fig. S2, the electrostatic model using the atomistic representations of the M13 capsid (1IFI three-dimensional structure, Fig. 2) is compared with the experimental cholesteric behavior of M13 virions. It turns out that the electrostatic model does not capture the experimentally-observed cholesteric assembly of M13 virions. If a left-handed helicity is predicted as observed experimentally, the large magnitude of the computed pitch $|P|$ evidences a strong underestimation of the chirality of the M13 cholesteric suspensions. A more detailed analysis of the electrostatic model based on the chiral potential of mean force reveals that the calculated cholesteric behavior may be attributed to the competition between the two distinct threads of the M13 virus capsids, which largely unwinds their preferred cholesteric pitch at higher densities (see Supplementary Section VI). In brief, the electrostatic model

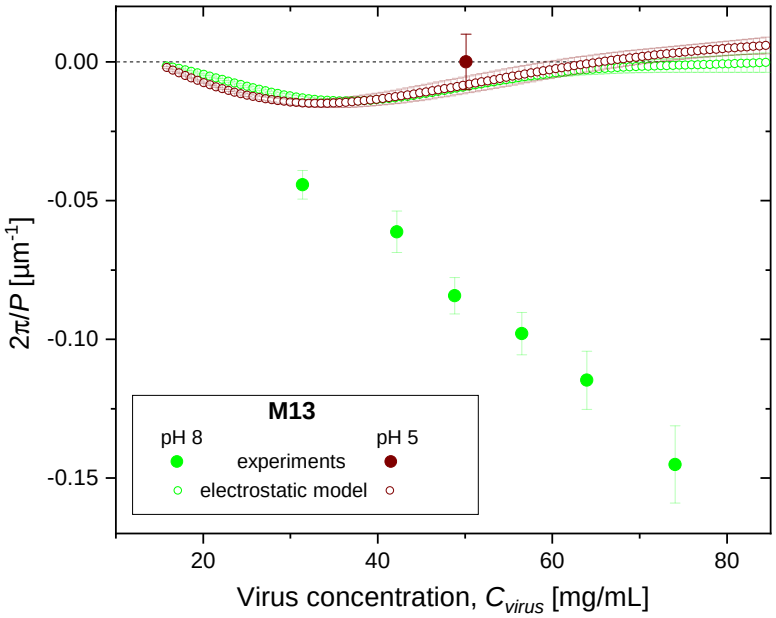

FIG. S2. **M13 virus suspensions and electrostatic model.** Inverse of cholesteric pitch P in suspensions of semi-flexible M13 viruses at low surface charge (pH 5, brown full symbol), and at high surface charge (pH 8, green full symbols), both at a fixed ionic strength of I_S=110 mM. Contrary to Y21M strain (Fig. 3), the electrostatic model (green open symbols) fails to account for the cholesteric behavior of the semi-flexible M13 phage at high pH. Error bars are determined as detailed in Methods.

has been shown to quantitatively account for the cholesleric phase formed by the Y21M strain (see main text and Fig. 3), but it fails to explain the cholesteric behavior of the semi-flexible M13 phage for which another mechanism of chirality transfer has therefore to be invoked (see the suprahelix model, as detailed in the main text).

IV. HARD HELICES: PITCH VS. RADIUS MODEL

The parametric equations of a right-handed helix of radius r, internal helical pitch h (Fig. 1), and oriented along the $\hat{\mathbf{z}}$ axis are

$$\begin{cases} x(t) = r\cos\dfrac{2\pi t}{h}, \\ y(t) = r\sin\dfrac{2\pi t}{h}, \\ z(t) = t, \end{cases} \tag{8}$$

for which the thread angle φ is defined as

$$\varphi = \arctan\frac{h}{2\pi r}. \tag{9}$$

The relation between the end-to-end distance L and the contour length L_c of the helix is given by

$$L^2 = \frac{L_c^2}{1+\left(\frac{2\pi r}{h}\right)^2} + 4r^2\sin^2\frac{\pi L_c}{h\sqrt{1+\left(\frac{2\pi r}{h}\right)^2}}. \tag{10}$$

In order to determine the end-to-end distance vs. contour length relationship for our viruses of persistence length L_p, we have to go beyond the simplest model provided by Kratky & Porod [13], which only holds for isolated polymeric chains. We thus examine the case of a filament within a narrow tube of diameter D, with $D \ll L_p$, as originally proposed by Odijk to introduce the concept of deflection length [14]. Here, the tube model provides a mean-field representation of the effective confinement induced by the crowded environment around a given rod-like virus in the (chiral) nematic phase, which presumably arises from short-ranged repulsive forces involving its nearest neighbors. For long chains such that $D \ll L_c$, the deflection length λ generally depends on the two relevant length scales D and L_p of the system, and is related to the deflection angle θ by

$$\theta \simeq \frac{D}{\lambda}, \tag{11}$$

valid in the limit of small θ.

Let us consider an elastic worm-like filament of contour length L_c, and denote by $\mathbf{r}(s)$ the position of an arbitrary chain segment at curvilinear abscissa s. We recall that in the absence of excluded-volume interactions, the orientational correlations of the chain decay exponentially,

$$\left\langle \mathbf{u}(s)\cdot\mathbf{u}(0)\right\rangle = \left\langle \cos\theta(s)\right\rangle = \exp\left(-\frac{s}{L_p}\right), \tag{12}$$

where $\langle\cdot\rangle$ denotes the canonical thermodynamic average, with $\mathbf{u}(s) \equiv d\mathbf{r}/ds$ the bond unit vector and $\theta(s)$ the angle between $\mathbf{u}(s)$ and $\mathbf{u}(0)$. In the stiff-rod limit, i.e. for $s \ll L_p$ and

small θ, we can expand Eq. (12) which yields for the mean square bending angle

$$\left\langle \theta^2(s) \right\rangle \simeq 2\frac{s}{L_p}. \tag{13}$$

Hence, for $s \equiv \lambda$, we obtain

$$\left\langle \theta^2 \right\rangle \simeq 2\frac{\lambda}{L_p} \simeq \left(\frac{D}{\lambda}\right)^2. \tag{14}$$

Eqs. (13) and (14) thus lead to a general expression of the deflection length λ in the scaling form

$$\lambda \simeq D^{2/3} L_p^{1/3}, \tag{15}$$

which corresponds to the typical curvilinear distance beyond which angular fluctuations deviate from those expected from Eq. (12) due to the steric constraints imposed by the surrounding nematic field. The squared end-to-end distance L^2 of the viral filament in the narrow tube then reads as

$$\begin{aligned} L^2 = \left[\mathbf{r}(L_c) - \mathbf{r}(0)\right]^2 &= \left[\int_0^{L_c} ds\, \mathbf{u}(s)\right] \cdot \left[\int_0^{L_c} ds' \mathbf{u}(s')\right] \\ &= \iint_0^{L_c} ds ds' \cos\theta(s'-s). \end{aligned} \tag{16}$$

Assuming θ to be a slowly-varying function of s for a stiff polymer, we may write

$$\cos\theta(s'-s) \simeq \cos\theta(s) + (s'-s)\frac{d\cos\theta(s)}{ds},$$

so that Eq. (16) may be recast in the form

$$L^2 \simeq L_c^2 \big\langle \cos\theta \big\rangle_c + \iint_0^{L_c} ds ds' (s'-s)\frac{d\cos\theta(s)}{ds}, \tag{17}$$

with $\langle\cdot\rangle_c$ the filament contour average,

$$\big\langle\, \cdot\, \big\rangle_c \equiv \frac{1}{L_c}\int_0^{L_c} ds\ \cdot .$$

The integration by parts of the last term in Eq. (17) leads to, after rearrangements,

$$L^2 \simeq 2L_c^2 \big\langle \cos\theta \big\rangle_c - \frac{L_c^2}{2}\big[\cos\theta(0) + \cos\theta(L_c)\big]. \tag{18}$$

In the long-chain limit ($D \ll L_c$), let us neglect potential end effects on the shape fluctuations of the filament, so that

$$\big\langle \cos\theta(s) \big\rangle \simeq \big\langle \big\langle \cos\theta \big\rangle_c \big\rangle \qquad \forall s \in [0, L_c].$$

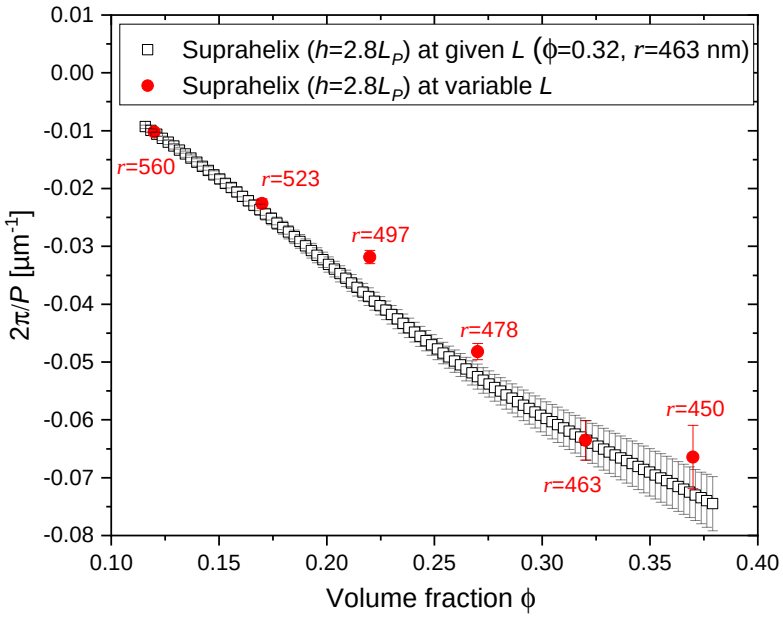

FIG. S3. **Cholesteric pitch P calculated by the suprahelix model** for M13-PEG system with $h = 2.8L_p$ when the explicit dependence of the virion effective length L with the volume fraction Φ is taken into account (full red dots for which each helix radius r, in nm, is indicated according to Eq. 10) and comparison with the calculation performed at fixed L for a given density $\Phi = 0.32$ (open black squares). As the difference between the two approaches is not significant, we may neglect the density variations of L for simplicity, and instead use a single fixed value over the entire concentration range, as plotted in Fig. 4b. Error bars are determined as detailed in Methods.

The thermal average of Eq. (18) then simply reads as

$$\langle L^2 \rangle \simeq L_c^2 \langle \cos\theta \rangle \simeq L_c^2 \left(1 - \frac{1}{2} \langle \theta^2 \rangle \right),$$

which yields, using Eqs. (14) and (15),

$$\langle L^2 \rangle \simeq L_c^2 \left[1 - \left(\frac{D}{L_p} \right)^{2/3} \right], \tag{19}$$

valid in the limit $D \ll L_p$ and $D \ll L_c$.

The tube diameter D is assumed to be twice the radial rod-to-rod distance δ_{inter}, which has been shown experimentally to behave as a 2D swelling law [15] according to

$$\delta_{\text{inter}}^2 = \frac{\pi}{2\sqrt{3}} d^2 \Phi^{-1}, \tag{20}$$

where d and Φ are the respective rod diameter and volume fraction. Plugged into Eq. (19) with $D \sim 2\delta_{\text{inter}}$, this gives

$$\left\langle L^2 \right\rangle \simeq L_c^2 \left[1 - \left(\frac{2\pi}{\sqrt{3}} \left(\frac{d}{L_p} \right)^2 \Phi^{-1} \right)^{1/3} \right], \tag{21}$$

or equivalently, by using the definition of the volume fraction $\Phi = \rho\, v_0 = C_{virus} N_A / M_w \times \pi L_c d^2/4$ where N_A is Avogadro's number, M_w the virus molecular weight, ρ the rod number density and v_0 the virus volume,

$$\left\langle L^2 \right\rangle \simeq L_c^2 \left[1 - \left(\frac{8}{\sqrt{3}} \left(\frac{M_w}{N_A C_{virus} L_c L_p^2} \right)^2 \right)^{1/3} \right], \tag{22}$$

independent of the virus diameter d.

Note that numerically, roots of Eq. (21) exist for helical pitches such that $h \lesssim L_p/2$. According to Eqs. 10 and 22, the resulting suprahelical virion backbone deformation may then be expressed in terms of the internal pitch h as the sole adjustable parameter for a given virion persistence length L_p, and at fixed rod packing fraction. Considering all the approximations of the model and more importantly, the fact that our hard helices are not strictly speaking flexible but represent a mean conformation, we choose to only keep the first term of Eq. (10) to make the pitch vs. radius relationship more tractable from a numerical point of view. Additionally, since the computed cholesteric pitches are found to be rather insensitive to the variations of the virion end-to-end distance L with the volume fraction Φ (see Fig. S3), we further neglect the density dependence of L in Eq. (21). This simplified approach is sufficient to properly account for the experimental data, as shown in Fig. 4b.

The sole "free" parameters of our model is the coefficient α relating the internal helical pitch of the helix with the persistence length, i.e. $h = \alpha L_p$. The optimization of α to account for the experimental data as reported in Fig. 4b is shown in Fig. S4, where we observe that the chirality of the cholesteric phase — i.e. the inverse of the cholesteric pitch $|P|$ — increases by increasing the curliness of the helix at given contour and persistence lengths, L_c and L_p.

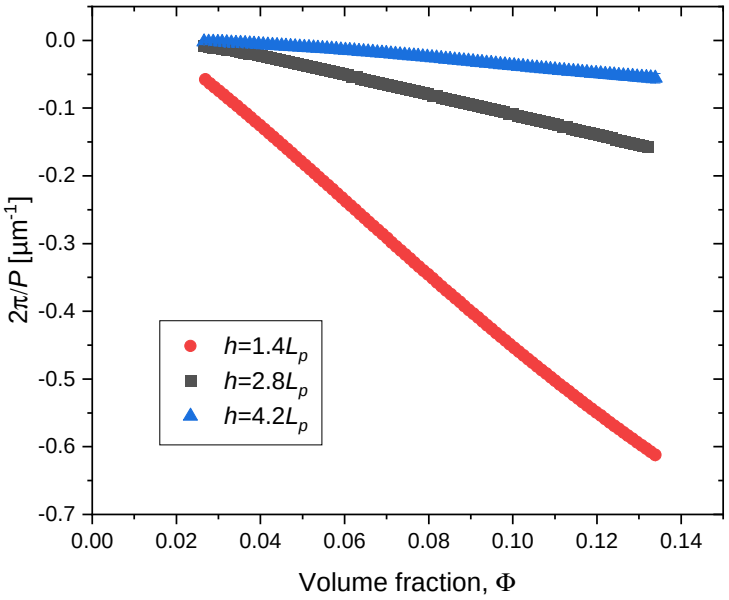

FIG. S4. **Suprahelix model dependence with the internal helicity** calculated at given contour length $L_c = 0.995$ μm and persistence length $L_p = 2.8\mu$m. The chirality of the cholesteric phase increases by decreasing the internal helical periodicity h of the helix.

V. SCALING BEHAVIOR OF HARD-HELIX CHOLESTERICS

Let us show that the equilibrium cholesteric pitch P of hard helices with fixed length L_c and radius r may be expressed as a unique function of the reduced volume fraction $\Phi/\Phi_{\rm iso}$. In the limit of weak helicity ($r \ll h$), we expect the local orientation distribution function ψ of the system to closely match that $\psi^{\rm cyl}$ of a straight cylinder with identical dimensions. In the context of Onsager theory [4], for $L_c \gg d$, the equilibrium shape of $\psi^{\rm cyl}$ is entirely controlled by the dimensionless parameter $\rho L_c^2 d \propto \Phi L_c/d$, where ρ is the molecular number density and $\Phi \equiv \rho\pi L_c d^2/4$ is the corresponding volume fraction. Thus,

$$\psi_{\rm eq} = \psi_{\rm eq}^{\rm cyl}\left(\Phi\frac{L_c}{d};\,\theta\right) \equiv \psi_{\rm eq}\left(\frac{\Phi}{\Phi_{\rm iso}};\,\theta\right), \tag{23}$$

where we use for the binodal volume fraction $\Phi_{\rm iso} \propto d/L_c$, and θ denotes the angle between the long axis of a helical particle and the local nematic director.

In this case, using Eq. (3), it may be shown that the Frank twist modulus K_{22} of such "rod-like" helices may be cast in the form [16, 17]

$$\beta K_{22} = \rho^2 L_c^4 d \times \mathscr{L}_2\big[\dot{\psi}_{\rm eq}\big], \tag{24}$$

with $\beta \equiv 1/k_B T$ the inverse temperature and $\dot{\psi}_{\rm eq}$ the first derivative of $\psi_{\rm eq}$ with respect to its angular argument. In Eq. (24), the functional $\mathscr{L}_2$ takes the form of a geometrical integral over all angular degrees of freedom describing the mutual orientations of pairs of overlapping particles [12, 16] (c.f. Eq. (3)), and is such that Eq. (24) simply reduces to Eq. (6) in the limit of strong orientational order. Thus, it follows from Eq. (23) that

$$\mathscr{L}_2\big[\dot{\psi}_{\rm eq}\big] \equiv M_2\bigg(\frac{\Phi}{\Phi_{\rm iso}}\bigg), \tag{25}$$

where the dimensionless scaling function M_2 is independent of the molecular geometry in the limit $L_c \gg d$ [16]. Using Eqs. (24) and (25), we may write

$$d\beta K_{22} \propto \Phi^2 \frac{L_c^2}{d^2} \times M_2\bigg(\frac{\Phi}{\Phi_{\rm iso}}\bigg) \propto \bigg(\frac{\Phi}{\Phi_{\rm iso}}\bigg)^2 M_2\bigg(\frac{\Phi}{\Phi_{\rm iso}}\bigg). \tag{26}$$

Hence, the twist modulus $d\beta K_{22}$, rescaled by the particle diameter d, may be written as a function of the sole reduced packing fraction $\Phi/\Phi_{\rm iso}$.

Analogously, in the case of shallow-grooved hard helices ($r \ll h$), the chiral strength K_t (Eq. (4)) may be approximated as [17]

$$\beta K_t = \rho^2 L_c^2 d\delta_0 \times \mathscr{L}_t\big[\psi_{\rm eq}, \dot{\psi}_{\rm eq}\big] \equiv \rho^2 L_c^2 d\delta_0 \times M_t\bigg(\frac{\Phi}{\Phi_{\rm iso}}\bigg),$$

with $\delta_0 \propto r$ the typical groove depth. Thus, we obtain

$$d\beta K_t \propto \Phi^2 \frac{\delta_0}{d^2} \times M_t\bigg(\frac{\Phi}{\Phi_{\rm iso}}\bigg) \propto \frac{\delta_0}{L_c^2} \times \bigg(\frac{\Phi}{\Phi_{\rm iso}}\bigg)^2 M_t\bigg(\frac{\Phi}{\Phi_{\rm iso}}\bigg). \tag{27}$$

Using Eqs. (26) and (27), the equilibrium cholesteric pitch P reads as

$$P \propto \frac{K_{22}}{K_t} \propto \frac{L_c^2}{\delta_0} \times Q\bigg(\frac{\Phi}{\Phi_{\rm iso}}\bigg), \tag{28}$$

where the scaling function $Q \equiv M_2/M_t$ is independent of molecular dimensions for $L_c \gg d$ and $r \ll h$. Note that for weakly-curved suprahelices with $h \gg L_c$, corresponding to finite fractions of full helices, the thread can *a priori* be a function of the helix contour length L_c, such that $\delta_0 \equiv \delta_0(L_c)$. Thus the dependence of the cholesteric pitch on the virus length cannot be trivially predicted from Eq. (28) in our case, which led us to analyze in more details these variations in Section VII.

For M13 viruses, we assume that PEGylation may affect the effective diameter d of the particles, but has only a limited impact on their overall contour length L_c and the magnitude

δ_0 of their helical fluctuations. Eq. (28) then imposes that P depends solely on $\Phi/\Phi_{\rm iso}$, in agreement with the observed experimental behavior of PEGylated viruses (Fig. 5 of the main text). Furthermore, in light of the vanishingly-small values of $2\pi/P$ associated with the electrostatic model of ground-state M13 conformations (Fig. 3 of the main text), we postulate that the effects of the detailed chiral surface charge distribution on the cholesteric assembly of thermalized viruses may be neglected. We may then simply consider the viruses as uniformly-charged (helical) rods, whose liquid-crystalline behavior can be remapped to that of a hard-body system with a charge- and ionic-strength-dependent effective diameter $d_{\rm eff} > d$ [18, 19]. Since Eq. (28) is independent of d, we thus expect the cholesteric pitch of bare viruses to be determined by the same unique function of $\Phi/\Phi_{\rm iso}$ as their PEGylated counterparts, regardless of ionic strength — which is consistent with the predictions of the suprahelix model (Fig. 5 of the main text). Thus, the collapse of our experimental data onto a single master curve evidences the irrelevance of the local symmetry of the surface charge distribution for the cholesteric phase of M13 viruses — and demonstrates that the origin of their chirality instead lies in long-wavelength helicoidal deformation modes, which are not significantly affected by PEGylation or changes in ionic conditions.

VI. CHIRAL POTENTIAL OF MEAN FORCE

In order to predict the thermodynamically-favored handedness in supramolecular assemblies of chiral particles, it is convenient to introduce the so-called *chiral potential of mean force* (PMF) [8, 20]. Let us consider a pair of viral particles with arbitrary orientations $\mathcal{R}_1$, $\mathcal{R}_2$ and center-of-mass separation $\mathbf{r}_{12}$, and denote by $\theta_{12} \equiv \arccos(\mathbf{u}_1 \cdot \mathbf{u}_2)$ the angle between the respective virus long axes $\mathbf{u}_1$ and $\mathbf{u}_2$. Using the notations of Section I, we define the pairwise angular PMF associated with right- and left-handed two-particle configurations via [8]

$$\overline{U}_{\pm}(\theta_{12}) \equiv -k_B T \, \log \left\langle e^{-\beta U_{\rm inter}} \right\rangle_{\pm}^{(\theta_{12})}, \tag{29}$$

with $\left\langle \, \cdot \, \right\rangle_{\pm}^{(\theta)}$ a chiral spatial and angular average,

$$\left\langle F \right\rangle_{\pm}^{(\theta)} \equiv \frac{1}{\Omega_{\pm}} \int_V d\mathbf{r}_{12} \oiint d\mathcal{R}_1 d\mathcal{R}_2 \, F(\mathbf{r}_{12}, \mathcal{R}_1, \mathcal{R}_2) \, \delta(\mathbf{u}_1 \cdot \mathbf{u}_2 - \cos\theta) \Theta\big\{ \pm \mathbf{r}_{12} \cdot (\mathbf{u}_1 \times \mathbf{u}_2) \big\} \tag{30}$$

for any function F of the configurational degrees of freedom $\mathbf{r}_{12}$, $\mathcal{R}_1$ and $\mathcal{R}_2$. In Eq. (30), Θ is the Heaviside step function, such that the $\pm$ subscript denotes an integral over all right-

(resp. left-) handed arrangements, characterized by $\mathbf{r}_{12} \cdot (\mathbf{u}_1 \times \mathbf{u}_2) > 0$ (resp. < 0), and $\Omega_\pm$ represents the total volume of the phase space associated with virus pair configurations of fixed handedness,

$$\Omega_\pm = \frac{(8\pi^2)^2}{2} V.$$

Using Eqs. (29) and (30), a system of two particles with fixed inter-axis angle θ_{12} may adopt a thermodynamically-stable right-handed configuration if the net repulsion associated with such an arrangement is lower than that of the respective left-handed structure — i.e., if $\overline{U}_+(\theta_{12}) < \overline{U}_-(\theta_{12})$. Reciprocally, $\overline{U}_+(\theta_{12}) > \overline{U}_-(\theta_{12})$ indicates a greater favorability of left-handed assemblies. The relative stability of helical supramolecular structures is thus quantified by sign of the chiral component of the PMF,

$$\Delta_c \overline{U}(\theta) \equiv \overline{U}_+(\theta) - \overline{U}_-(\theta) = k_b T \log \frac{\left\langle e^{-\beta U_{\text{inter}}} \right\rangle_-^{(\theta)}}{\left\langle e^{-\beta U_{\text{inter}}} \right\rangle_+^{(\theta)}}. \tag{31}$$

We report in Fig. S5 the angular variations of $\Delta_c \overline{U}$ for the various molecular systems considered in the main text. In the case of electrostatic model applied to Y21M (2C0W capsid structure, Fig. S5a), we find that $\Delta_c \overline{U}$ bears a unique minimum $\Delta_c \overline{U}_{\text{min}} < 0$ near inter-axis angles $\theta_{\text{min}} \simeq 70^\circ$, indicating that the optimal close-packing of the viruses may be achieved in a strongly-twisted right-handed configuration — consistent with the large primary thread angle $\varphi \simeq 43.15^\circ < 45^\circ$ inferred from the molecular symmetries of the capsid (see Figs. 1-2 and Extended Data Fig. 2a). Such purely geometric considerations — which mirror the seminal work of Straley [5], as illustrated in Extended Data Fig. 2 — generally need to be interpreted with caution, since the large value of θ_{12} associated with this close-approach arrangement is typically incompatible with the local orientational alignment characterizing the cholesteric phase [21], and further neglect the role of the angular fluctuations underpinning liquid-crystalline assemblies [1]. However, a closer inspection of Fig. S5a reveals that $\Delta_c \overline{U}_{\text{min}}$ is also associated with a regime of weakly-negative values of $\Delta_c \overline{U}$ at smaller twist angles $0 < \theta_{12} < \theta_{\text{min}}$, which encompasses the relative orientations more realistically sampled by close-neighbor rods in a standard cholesteric system [21] — and thus provides a simple explanation for the stability of the observed right-handed phase (see Fig. 3 and Extended Data Fig. 1b).

Conversely, for the M13 electrostatic (1IFI) model displaying a more complex helical charge distribution (Fig. 2), we remark that $\Delta_c \overline{U}$ exhibits a drastically-different and strongly

non-monotonic profile (Fig. S5b), in which the global minimum $\Delta_c\overline{U}_{\min} < 0$ around $\theta_{\min} \simeq 70^\circ$ is now associated with an intermediary peak $\Delta_c\overline{U}_{\max} > 0$ near $\theta_{\max} \simeq 45^\circ$, along with a local minimum $\Delta_c\overline{U}_{\rm loc} < 0$ at smaller angles $\theta_{\rm loc} \simeq 20^\circ$. We attribute this more complex behavior to the interplay between the primary and secondary threads identified from the M13 capsid structure (Figs. 1-2). Indeed, a simple extrapolation of the geometric argument in Extended Data Fig. 2 suggests that the mutual alignment of the primary groove of a given virus, of thread angle $\varphi \simeq 39.85^\circ$, with the secondary groove $\psi \simeq 5.15^\circ$ of a neighboring capsid (Figs. 1-2) gives rise to a left-handed close-approach configuration with twist angle $\theta_{12} = \varphi + \psi$ — thus accounting for the peak in $\Delta_c\overline{U}$ around $\theta_{\max} \simeq 45^\circ$, or equivalently $\theta_{\min} \simeq -45^\circ$. In this context, the local minimum near $\theta_{\rm loc} \simeq 20^\circ$ likely proceeds from the competition between the large-angle propensity for left-handed arrangements and the broader angular preference for right-handed assemblies resulting from the interactions between the capsid primary threads (c.f. Fig. S5a).

The non-monotonic dependence of the 1IFI cholesteric pitch on virus concentration (Fig. 3) may then be interpreted as follows. The larger orientational fluctuations associated with lower particle densities, which stem from the weaker degree of local alignment, may enable vicinal capsids to sample a regime of wider inter-axis angles, in which left-handed configurations are typically more favorable — as evidenced by the intermediary peak in $\Delta_c\overline{U}$ (Fig. S5b). Such configurations are however progressively precluded at higher concentrations, for which the viruses may be restricted to a regime of increasingly-small relative angles, at which right-handed configurations become increasingly stable. Thus, the left-handed cholesteric phase obtained near the isotropic-to-nematic transition point, along with its subsequent unwinding observed at higher densities (Fig. 3), may ensue from the antagonistic interplay between left- and right-handed particle arrangements — which arises from subtle, concentration-dependent variations in their local orientational fluctuations.

In the case of the M13 suprahelix model, the inclusion of the weakly-solenoidal backbone deformation instead leads to the appearance of a single minimum $\Delta_c\overline{U}_{\min} < 0$ (Fig. S6), indicating a unequivocal preference for left-handed phases — as expected from such weakly-curled, right-handed helical conformations with effective thread angles $\phi \gg 45^\circ$ (Figs.1 & 2 and Extended Data Fig. 2). The magnitude of this peak for PEGylated viruses is further found to be nearly tenfold larger than that of the corresponding extrema of $\Delta_c\overline{U}$ for the electrostatic model (Fig. S5b), suggesting that this large-scale helicity dominates cholesteric

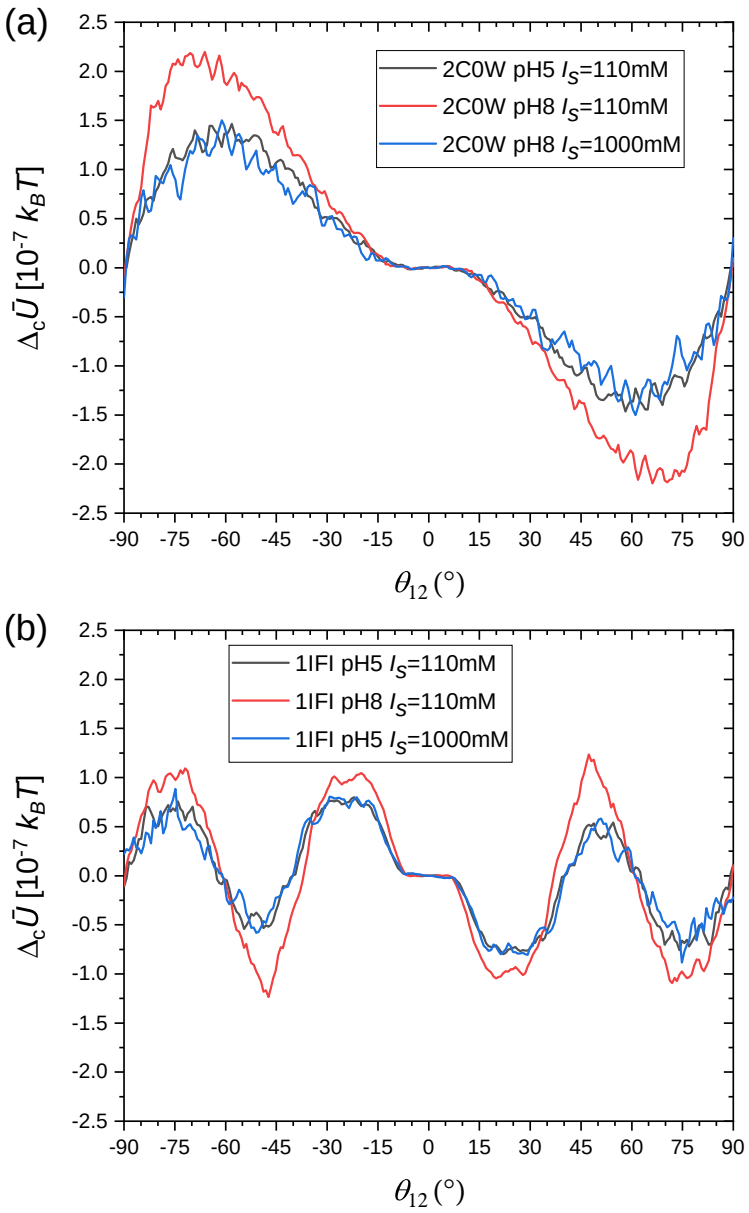

FIG. S5. **Chiral potential of mean force**, $\Delta\bar{U}_c$, as a function of the virus inter-axis angle, θ_{12}. $\Delta\bar{U}_c$ is calculated by integration of the pair potential over its spatial and angular degrees of freedom, for the electrostatic model of the (a) 2C0W (Y21M) and (b) 1IFI (M13) capsid structures at various pH and ionic strengths.

assembly over the local surface structure and charge distribution of the capsid. This observation reflects the conclusions of previous studies of DNA-origami-based liquid crystals [8], and is corroborated by the near-identical variations of $\Delta_c\overline{U}$ for PEGylated and unPEGylated models of M13 viruses (Fig. S6, blue and black lines), confirming that the obtained behavior

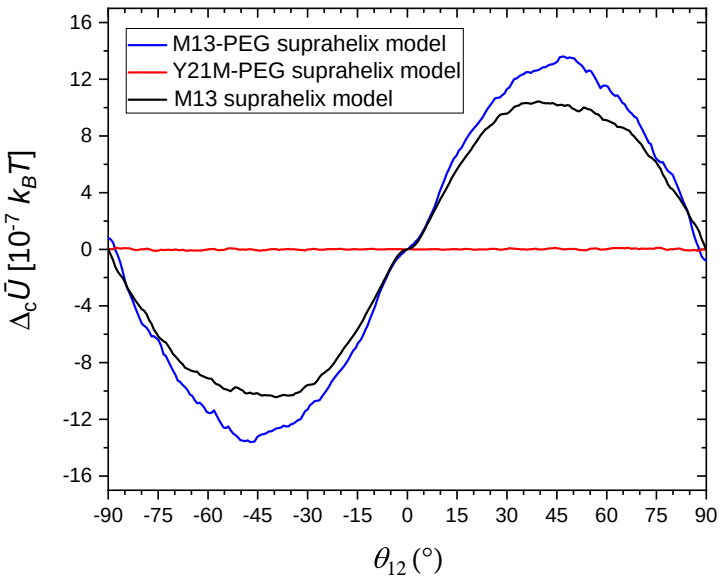

FIG. S6. **Chiral potential of mean force**, $\Delta\bar{U}_c$, as a function of the virus inter-axis angle, θ_{12}, for the suprahelix model of PEGylated phages (blue and red lines for M13-PEG and Y21M-PEG, respectively), as well as for unPEGylated M13 virions.

is now largely insensitive to the detailed atomic composition of the system. However, for Y21M variants, the larger bending rigidity L_p translates into a weaker solenoidal conformation of the backbone (see Sec. IV), which provides a negligible contribution to the chiral PMF (Fig. S6, red line). Thus, the cholesteric assembly of Y21M is chiefly governed by short-ranged electrostatic interactions driven by the local surface symmetries of the capsid.

VII. VIRUS LENGTH DEPENDENCE OF THE CHOLESTERIC PITCH

As detailed in Supplementary Section IV, the internal pitch $h = 2.8L_p$ of the helical fluctuations underlying the suprahelix model typically far exceeds the contour length L_c of the capsid ($h/L_c \simeq 8$ for M13, $h/L_c \simeq 30$ for Y21M), implying that these subtle deformations at the scale of an individual virion may only span a small fraction of a full helical period, as illustrated in Fig. 2. In this context, the following question arises: how is the resulting cholesteric pitch affected by altering the full contour length of the viruses? For this purpose, we exploit the genetic versatility of filamentous bacteriophages to grow a mutant called M13K07, which is 20% longer than the semi-flexible M13KE (referred to as M13 throughout the paper). Both viruses are monodisperse in size, but M13K07 exhibits a contour length

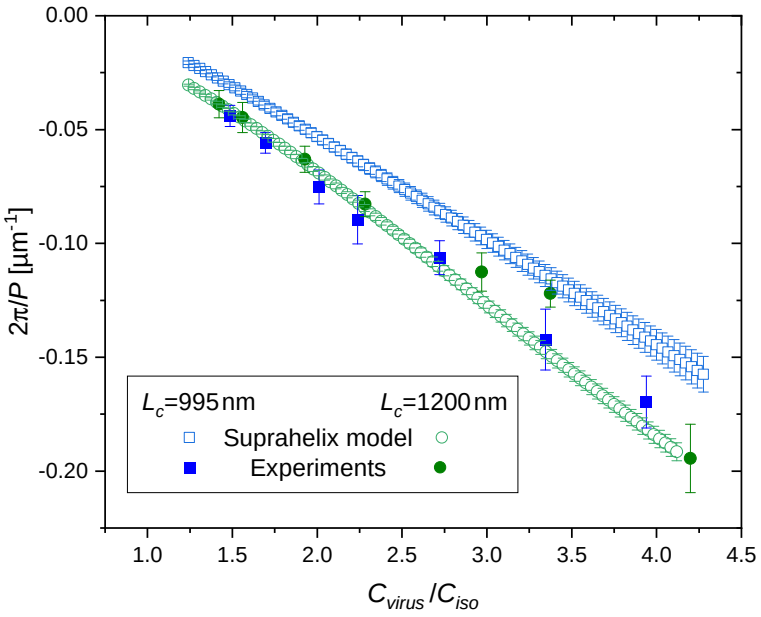

FIG. S7. **Virus length dependence of the cholesteric pitch.** Inverse of cholesteric pitch P in suspensions of M13 (blue squares) and M13K07 (green circles) viruses of respective contour length $L_c^{M13} = 995$ nm and $L_c^{M13K07} = 1200$ nm. For both strains, the persistence length is assumed to be identical, i.e. $L_p = 2.8$ μm, considering the similar structure of the two phages. Experimental data (full symbols) are measured at pH 8 and I_S=60 mM [22]. The suprahelix model (open symbols) with $h = 2.8L_p$ and with the binodal value C_{iso} corrected for the rod flexibility [23] is in reasonable agreement with the measured cholesteric pitches considering the experimental error bars. Error bars are determined as detailed in Methods.

of $L_c^{M13K07} = 1200$ nm. As the local structure of the virus remains unchanged, these two mutants only differing by their length, are assumed to have the same persistence length of $L_p = 2.8$ μm. Experimental measurements are shown in Fig. S7 and compared against the results of the suprahelix model computed for the two different phage lengths. The simulated cholesteric pitch $|P|$ is found to tighten by increasing the rod length, and is consistent with the experimental data within the error bars. This observation gives further support to the steric-based suprahelix model, in which the more pronounced helical shape of the longer variants (with smaller h/L_c) is expected to increase the chirality of their cholesteric phase in otherwise identical assembly conditions. These findings also qualitatively mirror

the conclusions of recent studies of fractionated cellulose suspensions [24], thus suggesting that such steric modes of chirality transfer may find broader potential applications within a wider class of experimental colloidal systems.

[1] Pierre-Gilles de Gennes and Jacques Prost. *The Physics of Liquid Crystals*. Clarendon Press, Oxford, 1993.

[2] Fabio Tombolato, Alberta Ferrarini, and Eric Grelet. Chiral nematic phase of suspensions of rodlike viruses: left-handed phase helicity from a right-handed molecular helix. *Phys. Rev. Lett.*, 96(25):258302, 2006.

[3] Maxime M. C. Tortora and Jonathan P. K. Doye. Perturbative density functional methods for cholesteric liquid crystals. *J. Chem. Phys.*, 146(18):184504, 2017.

[4] Lars Onsager. The effects of shape on the interaction of colloidal particles. *Ann. N.Y. Acad. Sci.*, 51(4):627–659, 1949.

[5] Joseph P. Straley. Theory of piezoelectricity in nematic liquid crystals, and of the cholesteric ordering. *Phys. Rev. A*, 14(5):1835, 1976.

[6] Judith Herzfeld, Alan E. Berger, and John W. Wingate. A highly convergent algorithm for computing the orientation distribution functions of rodlike particles. *Macromolecules*, 17(9):1718–1723, 1984.

[7] Maxime M. C. Tortora and Jonathan P. K. Doye. Hierarchical bounding structures for efficient virial computations: Towards a realistic molecular description of cholesterics. *J. Chem. Phys.*, 147(22):224504, 2017.

[8] Maxime M. C. Tortora, Garima Mishra, Domen Prešern, and Jonathan P. K. Doye. Chiral shape fluctuations and the origin of chirality in cholesteric phases of dna origamis. *Science Advances*, 6(31):eaaw8331, 2020.

[9] Maxime M. C. Tortora. High-performance density functional calculations for cholesteric liquid crystals. *chiralDFT*, https://doi.org/10.5281/zenodo.10823273, 2024.

[10] Zvonimir Dogic and Seth Fraden. Cholesteric phase in virus suspensions. *Langmuir*, 16(20):7820–7824, 2000.

[11] Massimo Bagnani, Paride Azzari, Cristiano De Michele, Mario Arcari, and Raffaele Mezzenga. Elastic constants of biological filamentous colloids: estimation and implications on nematic and cholesteric tactoid morphologies. *Soft Matter*, 17:2158–2169, 2021.

[12] Theo Odijk. Elastic constants of nematic solutions of rod-like and semi-flexible polymers. *Liquid Crystals*, 1(6):553–559, 1986.

[13] O. Kratky and G. Porod. Röntgenuntersuchung gelöster fadenmoleküle. *Recl. Trav. Chim. Pays-Bas*, 68(12):1106–1122, 1949.

[14] Theo Odijk. Theory of lyotropic polymer liquid crystals. *Macromolecules*, 19(9):2313–2329, 1986.

[15] Eric Grelet and Richa Rana. From soft to hard rod behavior in liquid crystalline suspensions of sterically stabilized colloidal filamentous particles. *Soft Matter*, 12:4621, 2016.

[16] Joseph P Straley. Frank elastic constants of the hard-rod liquid crystal. *Phys. Rev. A*, 8(4):2181, 1973.

[17] Theo Odijk. Pitch of a polymer cholesteric. *J. Phys. Chem.*, 91(23):6060–6062, 1987.

[18] Alain Stroobants, Henk N. W. Lekkerkerker, and Theo Odijk. Effect of electrostatic interaction on the liquid crystal phase transition in solutions of rodlike polyelectrolytes. *Macromolecules*, 19(8):2232–2238, Aug 1986.

[19] Jianxin Tang and Seth Fraden. Isotropic-cholesteric phase transition in colloidal suspensions of filamentous bacteriophage fd. *Liquid Crystals*, 19(4):459–467, 1995.

[20] Henricus H. Wensink. Spontaneous sense inversion in helical mesophases. *Europhys. Lett.*, 107(3):36001, 2014.

[21] Zvonimir Dogic and Seth Fraden. *Soft Matter Vol. 2: Complex Colloidal Suspensions, edited by G. Gompper and M. Schick*. Wiley-VCH, Weinheim, 2006.

[22] Eric Grelet and Seth Fraden. What is the origin of chirality in the cholesteric phase of virus suspensions? *Phys. Rev. Lett.*, 90(19):198302, 2003.

[23] Zheng Yu Chen. Nematic ordering in semiflexible polymer chains. *Macromolecules*, 26(13):3419–3423, 1993.

[24] Camila Honorato-Rios and Jan P. F. Lagerwall. Interrogating helical nanorod self-assembly with fractionated cellulose nanocrystal suspensions. *Communications Materials*, 1(1):69, Sep 2020.